



The magmatism of Atienza (NW Iberian Chain, Spain): age, origin and architecture of the magmatic plumbing system

Urbez Majarena¹  · Carlos Galé^{1,2} · José Julián Esteban³ · Marceliano Lago¹ · Andrés Gil-Imaz¹

Received: 30 November 2021 / Accepted: 10 February 2023 / Published online: 15 March 2023
© The Author(s) 2023

Abstract

A sill covering an area of more than 15 km², several dykes up to 5 m thick and a volcanoclastic deposit crop out with similar petrology in the sector of Atienza (NW Iberian Chain, Spain). They consist of calc-alkaline porphyritic andesites with phenocrysts of plagioclase, amphibole, biotite, garnet and orthopyroxene. Based on U–Pb zircon analysis, an age of 290 ± 3 Ma (Sakmarian-Artinskian in the Cisuralian) has been calculated for this magmatism. The chemistry and geothermobarometry on amphibole crystals revealed crystallisation at different depths between 31 and 16 km, involving several events of magma recharge and fractional crystallisation. Magma ascent led to destabilisation of the amphibole crystals, their replacement by biotite, and the formation of thick microcrystalline coronas. Whole-rock trace element and isotopic compositions support a strong crustal influence in the origin of the magma. Crustal melting was produced by heating generated after lithospheric thinning, delamination, and asthenospheric rise produced after the uplift of the Variscan Orogen and the oroclinal folding of the Iberian Massif.

Keywords Magma dynamics · Amphibole · Sakmarian-Artinskian · Permian · Calc-alkaline · Iberian chain

El magmatismo de Atienza (NW de la Cordillera Ibérica): edad, origen y arquitectura del sistema magmático

Resumen

En el sector de Atienza (NW de la Cordillera Ibérica, España) aflora un sill de más de 15 km², varios diques de hasta 5 m de espesor y un depósito volcanoclástico. Todos ellos están constituidos por andesitas porfídicas calco-alcálicas con fenocristales de plagioclasa, anfíbol, biotita, granate y ortopiroxeno. La edad de este magmatismo, en base a las relaciones U-Pb de

✉ Urbez Majarena
urbezmajarena@unizar.es

Carlos Galé
carlos.gale@gmail.com

José Julián Esteban
jj.esteban@ehu.es

Marceliano Lago
marceliano64@gmail.com

Andrés Gil-Imaz
agil@unizar.es

¹ Department of Earth Sciences-IUCA, University of Zaragoza, C/Pedro Cerbuna 12, 50009 Saragossa, Spain

² Área de Geología, IDEYA, Avda. de la Autonomía 7, 50003 Saragossa, Spain

³ Department of Geology, Faculty of Science and Technology, University of the Basque Country (UPV/EHU), Barrio Sarriena s/n. 48940, Leioa, Spain

los circones que contiene, es de 290 ± 3 Ma (Sakmariense-Artinskiense, Cisuraliense). El estudio composicional y geotermobarométrico de los cristales de anfíbol indica que su cristalización se produjo a diferentes profundidades entre 31 y 16 km e involucró diversos procesos de recarga magmática y cristalización fraccionada. El ascenso del magma produjo la desestabilización de los cristales de anfíbol, su reemplazamiento por biotita y la formación de coronas microcristalinas. La composición isotópica y de elementos traza de estas rocas indica una fuerte influencia cortical en el origen del magma. Los procesos de fusión de corteza fueron favorecidos por el calor generado por el ascenso astenosférico tras el adelgazamiento y delaminación litosférica que tuvieron lugar a finales de la Orogenia Varisca.

Palabras clave Sistema magmático · anfíbol · Sakmariense-Artinskiense · Pérmico · calco-alcalino · Cordillera Ibérica

1 Introduction

During the Cisuralian, intense calc-alkaline magmatism of intermediate-felsic composition took place throughout the Iberian Massif (Fernández-Suárez et al., 2000; Gutiérrez-Alonso et al., 2011; López-Gómez et al., 2019). The magmatism developed in a context of transtensive tectonics during the end of the Variscan Orogeny and the beginning of a rifting stage, related to the Pangea break-up and the beginning of the opening of the Neo-Tethys ocean (Torsvik & Cocks, 2016; Wilson et al., 2004). In the north-eastern sector of the Iberian Massif, Permian calc-alkaline magmatism is widely represented throughout the Iberian Chain by hundreds of intrusions and volcanic deposits with compositions ranging from rhyolitic to basaltic andesites (Lago et al., 2004, 2005). Their emplacement was related to directional faults and pull-apart basins and was mainly subvolcanic in the form of dykes and sills. However, block and ash pyroclastic deposits and a plutonic body, the Loscos gabbro, are also exposed (Lago et al., 2004) (Fig. 1).

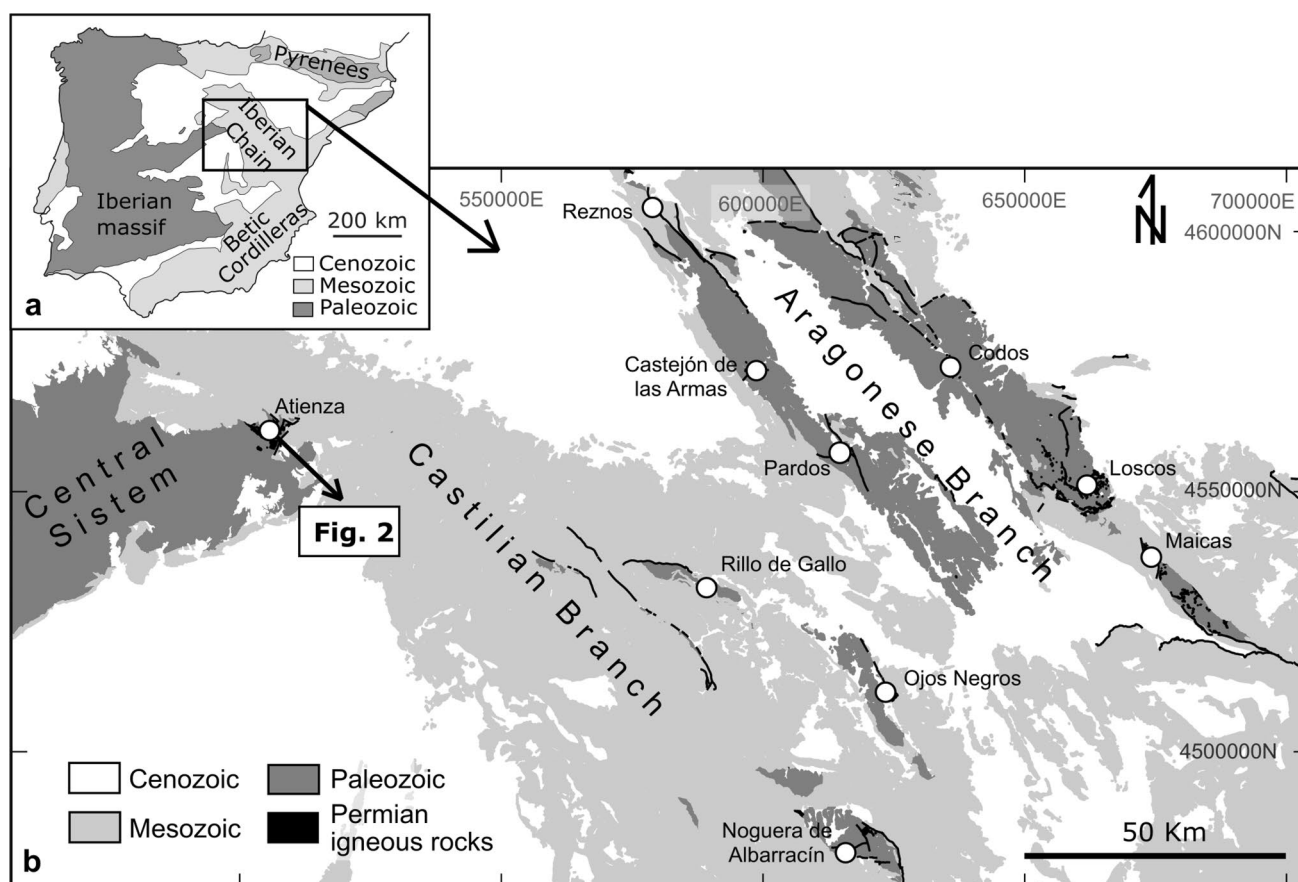


Fig. 1 Location of the studied area within the north-eastern sector of the Iberian Peninsula (a) and within the Iberian Chain (b). The white circles indicate the most representative outcrops of Permian magmatism in the Iberian Chain

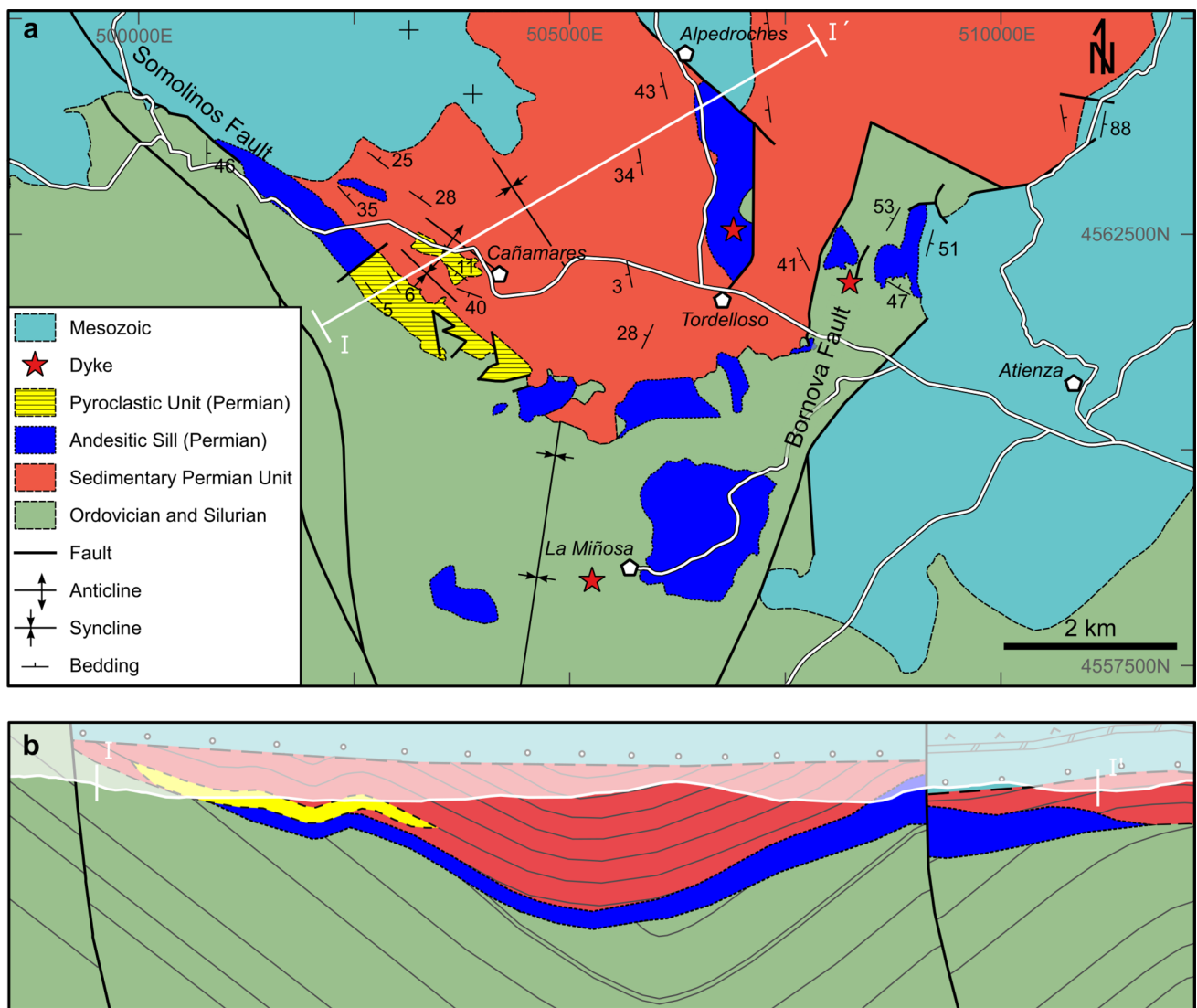


Fig. 2 Geological map (a) and cross-section (b) of the Atienza area

The sector of Atienza (Fig. 1, 2) hosts the highest volume of calc-alkaline Permian igneous rocks in the Iberian Chain. These rocks have been the subject of several studies about their position within the Permian stratigraphic series (Hernán et al., 1981; Hernando, 1980; Pérez-Mazarío, 1990; Virgili et al., 1973). The only radiometric dating of the Atienza magmatism was carried out by Hernando et al., (1980), with a result of 287 ± 12 Ma (Asselian-Kungurian) based on the $^{40}\text{K}/^{40}\text{Ar}$ whole-rock analysis. Ancochea et al. (1981) related the origin of this magmatism with the collision between continents during the Variscan Orogen. Finally, the geochemical composition of some of these rocks was part of a general study about the Permian calc-alkaline magmatism in the Iberian Chain (Lago et al., 2004).

None of these previous studies focused in detail on the evolution of the magmas from their origin to their

emplacement close to the surface, nor the magmatic processes recorded on these rocks, except for the assimilation of xenoliths (Aparicio & García-Cacho, 1984; Lago et al., 2004). The rocks of Atienza contain a complex phenocryst assemblage, including calcic amphibole that shows textures and zoning patterns suggesting a complex evolution in the P–T conditions of crystallisation. Recent studies highlight that amphibole composition is a very useful tool for unravelling magmatic processes such as magma storage, mixing and ascent since this mineral crystallises in a wide range of physicochemical and compositional conditions (Gorini et al., 2018 and references therein, Ubide et al., 2014).

In this work, we present a detailed petrological, mineralogical and compositional study of the Permian calc-alkaline magmatism of the Atienza sector. The geothermobarometric study of the amphiboles of these rocks unravels the processes

that occurred during the crystallisation of the magmas and makes it possible to reconstruct, for the first time, the architecture of a Permian magmatic system in the Iberian Chain. The new geochemical data and the isotopic compositions from Lago et al. (2004) allowed us to approach the origin of the melts. Finally, we present the first U–Pb zircon age of these rocks, which constrains the age of the magmatism to the Sakmarian–Artinskian.

2 Geological setting

The magmatism of Atienza is located in the Castilian Branch of the Iberian Chain (Fig. 1a, b), which represents the westward extension of the West Asturian Leonese Zone (WALZ) of the Iberian Massif (Álvarez, 1991; Álvarez et al., 2018; Calvín-Ballester & Casas, 2013; Julivert & Martínez, 1983; Tejero & Capote, 1987) and is in contact with the north-eastern part of the Spanish Central System (SCS), in the Central Iberian Zone (CIZ) (Fig. 1b).

In the study area, three lithostructural units can be recognised. A first Paleozoic unit, in the southern part, formed by Ordovician and Silurian rocks arranged in a large NNE–SSW oriented syncline (Fig. 2a) and belonging to the extreme SE part of the Ollo de Sapo Domain of the CIZ of the Iberian Massif (Martínez Catalán et al., 2004). This syncline is part of the Hiendelaencina anticlinorium, a Variscan structure resulting from several stages of deformation (Gabaldón et al., 1978). The second unit comprises Permian rocks that crop out in the central part of this area (Fig. 2a) and are disposed discordantly on the Silurian units (Fig. 2b). They form a syncline (Cañamares Syncline) with an NW–SE orientation except in the easternmost part (Fig. 2). The third unit comprises the Triassic succession, discordantly overlapping any of the previous units (Fig. 2).

The outcrops of igneous rocks locate in the confluence of two important faults of regional scale: the prolongation of the Somolinos fault, with an NW–SE strike, and the Bornova Fault of NNE–SSW strike (Fig. 2a). According to Hernando (1980), these two faults controlled the sedimentation during the Permian and allowed the rise of andesitic magmas, locating the thickest outcrop (outcrop of La Miñosa, Fig. 2) at the confluence between this two faults. The igneous outcrops of Atienza comprise one sill, a pyroclastic deposit and several dykes (Fig. 2).

The sill (Fig. 3a) measures more than 15 km² and intruded through the Permian base unconformity (Majarena et al., 2015b). Its thickness increases towards the east (Fig. 2b), exceeding 100 m at the contact between the prolongation of the Somolinos Fault (NW–SE strike) and the Bornova Fault (NNE–SSW strike) (Fig. 2a).

Southwest of Cañamares village, there is a volcanic succession (Fig. 2a) composed of tens of pyroclastic flows of block and ash (Fig. 3b). It has up to 80 m in thickness, shows irregular and very well-defined bedding surfaces (Fig. 3c), and contains numerous stems and leaves fossils of *Callipteris Conferta* carried by the pyroclastic flows (Lago et al., 2005, Fig. 3d). The deposit of each pyroclastic flow has a basal section with abundant blocks of cm to dm in size, and an upper part formed by ash-fall deposits with a very fine grain size that measures several centimetres thick or is completely eroded.

To the south of Alpedroches village, the sill is cross-cut by a set of dark grey dykes (Fig. 2a) with an N–S strike, sub-vertical dip, between 0.5 and 5 m in thickness (Fig. 3e) and net contacts (Fig. 3f). Moreover, two dykes intrude the Silurian series, one of them to the W of La Miñosa village and the other in the north-eastern sector of the studied area (Fig. 2a).

3 Methodology

For this study, polished thin sections of 22 rock samples (15 from the sill; 4 from the volcanic succession and 3 from the dykes), hundreds of mineral analyses of 14 rock samples (9 from the sill: ATU-2, ATU-4, ATU-9, ATU-10, ATU-11, ATU-12, AT-6, AT-12, AT-13; 2 from the volcanic succession: ATU-7, ATU-8; and 3 from the dykes: ATU-D1, ATU-D2 and ATU-D3; Supplementary material 1.), 10 whole-rock analyses (major and trace elements) from the less altered samples (7 from the sill: ATU-2, ATU-3, ATU-4, ATU-9, ATU-10, ATU-12 and ATU-13; 1 from the volcanic deposit: ATU-8; and 2 in the dykes: ATU-D1 and ATU-D2.), and tens of analyses of U–Pb in zircon crystals from a sample of the sill (ATUZ.), were made. We also consider the six whole-rock analyses (AT-06, AT-07, AT-08, AT-11, AT-12 and AT-13.) from Lago et al. (2004) from this sector, which include major and trace elements, and ⁸⁷Rb/⁸⁷Sr, ⁸⁷Sr/⁸⁶Sr, ¹⁴⁷Sm/¹⁴⁴Nd and ¹⁴³Nd/¹⁴⁴Nd ratios in four of them (AT-6, AT-8, AT-12 and AT-13.).

Polished thin sections were prepared at the *Servicio de Preparación de Rocas y Materiales Duros*, Universidad de Zaragoza (Spain). Mineral compositions were determined at the *Unidad de Fluorescencia y Microsonda Electrónica*, Universidad de Oviedo using a Cameca SX-50 electronic microprobe and at the *Centro Nacional de Microscopía Electrónica*, Universidad Complutense de Madrid (Spain) using a JEOL JXA-8900 M electronic microprobe. Back-scattered electron images of the samples were used to guide

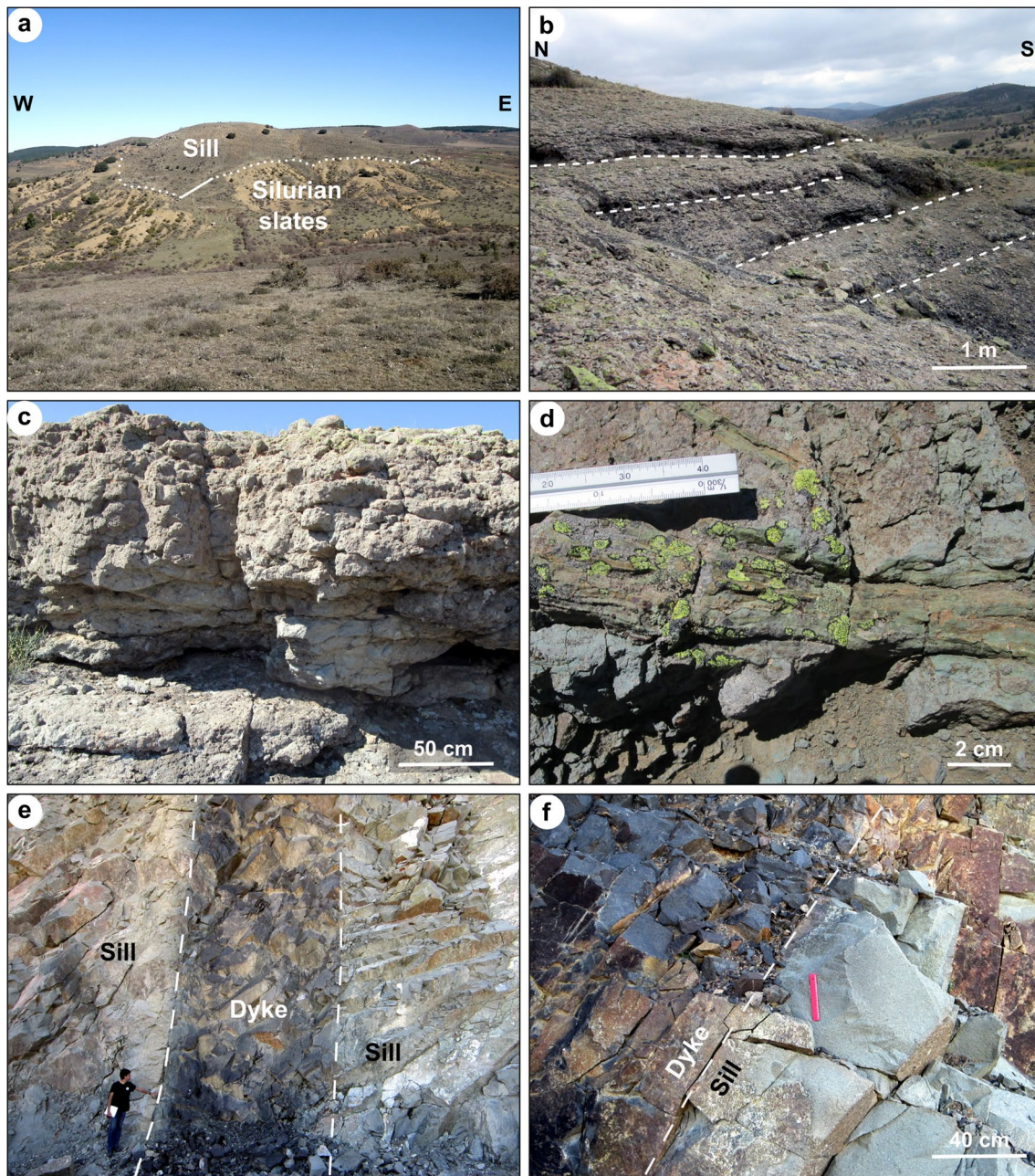


Fig. 3 Field photographs of the different igneous bodies. **a** Contact between the sill and the Silurian slates. **b** General appearance of the pyroclastic deposit. **c** Detail of the facies of the pyroclastic deposit. **d**

Fossil plant in the pyroclastic deposit. **e** Dyke cutting the sill. **f** Detail of the contact between the sill and one of the dykes

electron microprobe analysis. Analyses from Cameca SX-50 electronic microprobe were performed using an accelerating voltage of 15 kV and an electron beam current of 15 nA, with a beam diameter of 3 μm . Elemental counting times were 10 s on the peak and 5 s on each of the two background positions. The standards used were orthoclase (K, Si), wollastonite (Ca), albite (Na, Al), pyrophanite (Mn, Ti), hematite (Fe), strontianite (Sr), barite (Ba) and synthetic MgO , Cr_2O_3 , Rb_2O and NiO. Analyses from JEOL JXA-8900 M

electronic microprobe were performed using an accelerating voltage of 15 kV and an electron beam current of 20 nA, with a beam diameter of 5 μm . Elemental counting times were 10 s on the peak and 5 s on each of the two background positions. The standards used were albite (Na, Si), sillimanite (Al), almandine (Fe, Mn), microcline (K), kaersutite (Mg, Ca, Ti), fluorapatite (P, F, Cl) and pure metal (Ni, Cr). Precision was 0.8 to 5% for major and minor elements. All electron microprobe analyses were corrected for inter-elemental

effects using a ZAF (Z: atomic number; A: absorption; F: fluorescence) procedure.

Whole-rock analyses were carried out at the *SGIker-Geochronology and Isotopic Geochemistry Facility*, Universidad del País Vasco (Spain). The samples were run for major oxides and selected trace elements using an inductively coupled plasma-optical emission spectrometer (ICP-OES Perkin Elmer Optima 8300) and an inductively-coupled plasma mass spectrometer (ICP-MS X7 Thermo Scientific updated to XSeries 2). The procedures of analyses and standards are provided in Madinabeitia et al. (2008). Detection limits for major oxides were better than 0.0007 wt.% except for Na₂O (0.0015 wt.%). Detection limits for trace elements were better than 0.03 ppm except for Ba (0.19 ppm), Co (0.07 ppm), Cr (0.73 ppm), Cu (10.8 ppm), Ni (3.22 ppm), Rb (0.09), Sr (0.12), Pb (0.79 ppm), Zr (0.08 ppm) and Y (0.31 ppm). Measurements of geochemical reference standards were carried out to guarantee the quality and accuracy of the analyses.

The sample for zircon analyses (ATUZ,) was crushed in a steel jaw-crusher and sieved to select the fine fraction (<250 μm) at the *Servicio de Preparación de Rocas y Materiales Duros*, Universidad de Zaragoza (Spain). Zircon concentrates were obtained by using the Wilfley table and heavy liquids (methylene iodide) and selected zircon grains were mounted in epoxy resin. Electron back-scattering images were used to reveal the internal structures of the zircon grains and target areas for analysis. Analyses of zircons were conducted at the *SGIker-Geochronology and*

Isotopic Geochemistry Facility, Universidad del País Vasco (Spain). The samples were ablated with a 213 nm Nd: YAG-based laser ablation system (NewWave Research) coupled to a Thermo Fisher iCAP Qc quadrupole ICP-MS instrument with enhanced sensitivity through a dual pumping system. Analytical conditions involved spot diameters of 40 μm associated with repetition rates of 10 Hz and laser fluence at the target of ca. 2.5 J/cm². The ablated material was carried into helium, then mixed with argon and stabilized with a smoothing device (Tunheng & Hirata, 2004) before injection into the plasma source. Single analyses consisted of 25 s of background integration with the laser off followed by 45 s integration with the laser firing. Data reduction was carried out with Iolite v. 3.32 (Paton et al., 2011) and VizualAge (Petrus & Kamber, 2011) using the GJ-1 zircon standard (Jackson et al., 2004) for calibration and Plešovice zircon as secondary standard (Sláma et al., 2008). The analyses of the standards are shown in the Supplementary material 2. Tera-Wasserburg diagrams (Tera & Wasserburg, 1972) and weighted average age were produced using Isoplot/Ex 3.0 (Ludwig, 2003).

4 Results

4.1 Petrography

Both subvolcanic and volcanic rocks are intermediate rocks of grey colour and have porphyritic texture (Fig. 4a,

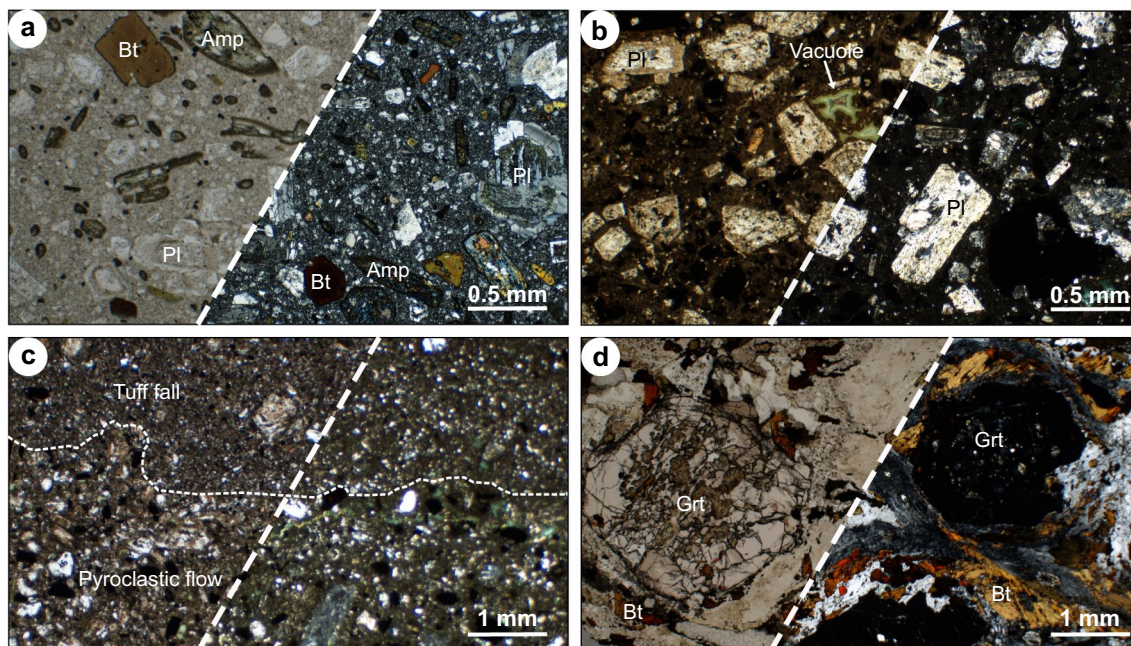


Fig. 4 Plane-polarized transmitted light photomicrographs of the samples dated in this study. **a** Subvolcanic rock. **b** volcanic (pyroclastic) rock. **c** Contact between a pyroclastic flow and an ash fall deposit. **d** Example of a garnet-biotite bearing metapelite xenolith

b) with about 40 vol.% phenocrysts of plagioclase (55 vol.%), amphibole (30 vol.%), biotite (13 vol.%), garnet (2 vol.%) and orthopyroxene (< 1 vol.%) (modal fractions calculated by visual estimation). These phenocrysts show different degrees of alteration, some replaced by chlorite, calcite, or opaque minerals. The volcanic rocks are more altered and have all the amphibole crystals replaced by the secondary phases described above. We have not observed differences in the degree of alteration between the dykes and the sill. All the studied samples also contain xenocrysts of quartz (< 1 vol.%) and some of them also contain xenoliths of black slates and metapelites up to 8 cm in size (< 2 vol.%).

The plagioclase phenocrysts reach 3.2 mm in size and have a subhedral habit and oscillatory zoning. Some crystals are strongly altered and completely replaced by secondary minerals. Occasionally, resorption horizons as those described by Ruprecht and Worner (2007), Smith et al. (2009) or Shcherbakov et al. (2011) truncate the layers of the oscillatory zoning. Some crystals show rounded cores surrounded by oscillatory zoning. Plagioclase microcrystals occur in the matrix and the amphibole coronas.

The amphibole crystals range between 0.2 and 2.2 mm in size and have subhedral to anhedral habits. Most amphiboles make up isolated phenocrysts and, in some cases, show cores (C-type) overgrown by mantles (M-type). Others appear grouped in glomeroporphyritic aggregates and show a zoning pattern (G-type). Most amphiboles have coronas formed by microcrysts of clinopyroxene, amphibole, plagioclase, biotite, ilmenite, magnetite, titanomagnetite and apatite. The rest of the amphiboles show resorbed textures.

The igneous biotite occurs as euhedral and homogeneous crystals up to 0.8 mm in size, as inclusions in amphibole, in pseudomorphs of amphibole and the coronas of the amphibole. On the other hand, some biotite crystals have anhedral habits and numerous inclusions, show darker colours in parallel polars and resorbed borders, and are similar to the biotite of the xenoliths.

Garnet can reach 1 cm. It shows cracked and mottled cores with inclusions of biotite, ilmenite, rutile and apatite. This textural feature is typical of the garnets from the metapelite xenoliths, and these cores have been interpreted as xenocrystic (Majarena et al., 2015a and 2021). The xenocrystic cores are surrounded by homogeneous mantles, without inclusions and with scarce cracks, that have been interpreted as of igneous origin (Majarena et al., 2015a and 2021).

The orthopyroxene and zircon are accessory minerals (< 1%). The orthopyroxene phenocrysts are between 0.2 and 1.2 mm long and have a subhedral habit. The zircons crystals are 150–400 µm long, euhedral to subhedral, with

straight edges and mainly prismatic. Finally, quartz forms rounded xenocrysts up to 0.8 mm in size.

The subvolcanic samples (sill and dykes) show an equigranular microcrystalline matrix (Fig. 4a) with quartz, plagioclase, minor apatite and, in a lower proportion, secondary opaque minerals.

The pyroclastic flows contain up to decimetre-sized juvenile fragments and isolated crystals (plagioclase, amphibole, biotite, quartz and garnet) immersed in an altered vitreous matrix with low contents in vesicles (Fig. 4b). The juvenile fragments are porphyritic andesites containing the crystals listed above in an equigranular microcrystalline matrix similar to that of the subvolcanic samples. The rocks corresponding to the fall deposits are made up of very fine-grained crystals and shards (Fig. 4c).

Metapelite xenoliths contain biotite, garnet, sillimanite, and orthoclase (Fig. 4d). This mineral association corresponds to the metamorphic facies of amphibolite (Bushmin & Glebovitsky, 2008). They have strongly resorbed edges and occasionally are interdigitated with the andesites that host them.

4.2 Whole-rock geochemistry

The analytical results of the whole-rock (major oxides, trace elements, and Sr–Nd isotopic composition) of the representative samples of this magmatism are listed in Table 1. The loss on ignition (LOI) ranges between 1.17 wt.% and 5.72 wt.%. The rocks with LOI > 4 wt.% (ATU-3, ATU-8, ATU-10 and AT-12; Table 1) show the main variability in the whole-rock composition and, for this reason, are not taken into account for the geochemical study.

SiO₂ contents range from 59.14 wt.% to 61.89 wt.% (volatile-free), Al₂O₃ from 16.82 wt.% to 17.89 wt.%, FeO_T from 4.21 wt.% to 5.21 wt.%, and TiO₂ from 0.53 wt.% to 0.76 wt.%. The rocks are sub-alkaline with Na₂O contents ranging from 3.46 wt.% to 4.95 wt.% and K₂O from 2.11 wt.% to 2.73 wt.%. Most of the samples plot in the High-K calc-alkaline series (Fig. 5a). The MgO contents range between 1.17 wt.% and 3.09 wt.% and the Mg* [Mg* = MgO / (MgO + Fe₂O₃ * 0.9) * 100] between 23.30 and 44.80. All rocks are peraluminous in composition with A/CNK values [Al₂O₃ / (CaO + Na₂O + K₂O) wt.%] ranging between 1.47 and 1.82 (Table 1). No significant correlation of SiO₂ with other major oxides (Supplementary material 3) and trace elements (not shown) has been detected.

The samples are classified as andesite, dacite, trachyandesite and trachyte on the TAS diagram (Fig. 5b) and as andesites on the Nb/Y–SiO₂ diagram (Fig. 5c). The rocks share a similar composition that is consistent with Permian calc-alkaline magmatism of the Iberian Chain (Lago et al., 2004 and references therein, Fig. 5).

Table 1 Major (wt.%), trace element (ppm) and isotopic composition of the studied rocks

| Sample | ATU-2 | ATU-3 | ATU-4 | ATU-8 | ATU-9 | ATU-10 | ATU-12 | ATU-13 | ATU-D1 | ATU-D2 | AT-06* | AT-07* | AT-08* | AT-11* | AT-12* | AT-13* |
|--------------------------------|---------|---------|---------|----------|---------|---------|---------|---------|---------|---------|---------|---------|---------|---------|---------|---------|
| X coord | 502327 | 502666 | 503568 | 503352 | 504593 | 507812 | 506899 | 505828 | 506894 | 506905 | 506269 | 503592 | 507053 | 508251 | 506742 | 506561 |
| Y coord | 4562276 | 4562965 | 4562206 | 4561247 | 4560556 | 4561213 | 4562550 | 4560576 | 4562545 | 4562556 | 4559007 | 4558580 | 4559489 | 4562393 | 4559479 | 4558876 |
| Type | Sill | Sill | Sill | Volcanic | Sill | Sill | Sill | Sill | Dyke | Dyke | Sill | Sill | Sill | Sill | Sill | Sill |
| SiO ₂ | 61.64 | 59.99 | 61.10 | 58.40 | 60.48 | 55.73 | 60.30 | 60.88 | 59.14 | 59.34 | 61.89 | 61.79 | 61.85 | 60.81 | 61.27 | 61.59 |
| TiO ₂ | 0.54 | 0.54 | 0.67 | 0.72 | 0.53 | 0.85 | 0.70 | 0.70 | 0.71 | 0.69 | 0.75 | 0.76 | 0.76 | 0.72 | 0.61 | 0.73 |
| Al ₂ O ₃ | 16.82 | 17.13 | 16.94 | 16.10 | 17.22 | 16.95 | 17.22 | 17.55 | 17.26 | 17.19 | 17.70 | 17.64 | 17.89 | 17.16 | 17.01 | 17.52 |
| Fe ₂ O ₃ | 4.21 | 3.61 | 4.80 | 5.35 | 4.23 | 6.20 | 4.96 | 4.28 | 4.81 | 4.87 | 4.99 | 5.21 | 4.93 | 4.35 | 4.03 | 5.02 |
| MnO | 0.03 | 0.03 | 0.07 | 0.06 | 0.03 | 0.10 | 0.08 | 0.05 | 0.05 | 0.07 | 0.18 | 0.18 | 0.19 | 0.08 | 0.04 | 0.07 |
| MgO | 3.05 | 3.86 | 1.99 | 4.23 | 3.09 | 3.10 | 2.41 | 1.17 | 2.10 | 2.27 | 2.51 | 2.50 | 2.46 | 1.94 | 1.57 | 2.04 |
| CaO | 3.31 | 1.73 | 4.62 | 1.49 | 3.39 | 5.78 | 3.70 | 4.53 | 4.88 | 5.13 | 4.30 | 4.23 | 4.25 | 4.57 | 4.23 | 4.60 |
| Na ₂ O | 3.46 | 1.88 | 4.09 | 2.16 | 3.64 | 3.47 | 4.95 | 3.79 | 4.55 | 3.95 | 3.50 | 3.59 | 3.59 | 3.98 | 3.30 | 4.52 |
| K ₂ O | 2.46 | 5.44 | 2.31 | 4.31 | 2.53 | 1.16 | 2.35 | 2.73 | 2.34 | 2.33 | 2.12 | 2.11 | 2.22 | 2.60 | 2.57 | 2.23 |
| P ₂ O ₅ | 0.17 | 0.18 | 0.28 | 0.27 | 0.18 | 0.35 | 0.28 | 0.32 | 0.29 | 0.29 | 0.21 | 0.20 | 0.21 | 0.20 | 0.18 | 0.21 |
| LOI | 3.42 | 4.37 | 2.11 | 5.72 | 3.43 | 5.35 | 1.95 | 2.77 | 2.62 | 2.66 | 1.48 | 1.53 | 1.42 | 3.34 | 4.84 | 1.17 |
| Total | 99.11 | 98.76 | 98.98 | 98.80 | 98.75 | 99.04 | 98.90 | 98.77 | 98.73 | 98.79 | 99.63 | 99.74 | 99.77 | 99.75 | 99.65 | 99.70 |
| Rb | 82.1 | 83.8 | 80.1 | 79.7 | 68.0 | 34.5 | 65.0 | 85.1 | 65.0 | 67.7 | 73.8 | 66.2 | 74.5 | 89.8 | 99.2 | 78.2 |
| Cs | 4.6 | 5.9 | 3.0 | 2.8 | 3.6 | 2.2 | 2.4 | 3.5 | 2.0 | 1.9 | 1.6 | 2.0 | 1.7 | 4.6 | 8.4 | 2.9 |
| Sr | 475.9 | 181.5 | 727.3 | 113.3 | 407.6 | 357.5 | 488.9 | 594.2 | 559.2 | 605.3 | 563.5 | 540.5 | 553.4 | 434.0 | 293.8 | 654.1 |
| Ba | 716.7 | 727.1 | 769.6 | 459.5 | 602.1 | 419.5 | 724.2 | 765.1 | 711.5 | 656.6 | 719.1 | 673.0 | 705.5 | 762.6 | 821.0 | 719.9 |
| V | 50.4 | 50.2 | 61.5 | 68.6 | 48.3 | 97.1 | 61.3 | 57.5 | 56.0 | 61.0 | 76.7 | 76.3 | 75.9 | 72.7 | 34.8 | 73.6 |
| Cr | 70.3 | 44.6 | 95.0 | 15.0 | 50.5 | 39.4 | 53.5 | 62.6 | 43.1 | 55.2 | 33.6 | 34.4 | 34.2 | 24.5 | 16.5 | 23.6 |
| Co | 9.2 | 11.6 | 9.8 | 9.6 | 7.7 | 13.0 | 8.9 | 7.6 | 8.7 | 8.7 | 10.0 | 10.9 | 10.0 | 10.2 | 7.7 | 9.6 |
| Ni | <BDL | <BDL | 4.0 | <BDL | <BDL | 5.1 | <BDL | <BDL | <BDL | <BDL | 10.6 | 8.4 | 8.3 | 9.5 | 6.2 | 7.1 |
| Cu | 21.1 | 33.4 | 13.5 | 11.4 | 11.8 | 23.3 | 12.7 | 37.6 | 14.2 | 12.3 | 22.2 | 7.0 | 22.4 | 11.8 | 9.8 | 3.9 |
| Y | 14.3 | 10.8 | 15.8 | 15.7 | 11.8 | 25.4 | 14.0 | 12.3 | 14.2 | 14.0 | 13.1 | 13.3 | 13.1 | 16.6 | 7.5 | 12.8 |
| Nb | 9.2 | 8.2 | 12.4 | 10.4 | 7.6 | 12.2 | 10.6 | 10.3 | 10.4 | 10.1 | 12.2 | 11.6 | 11.7 | 12.8 | 11.5 | 12.2 |
| Ta | 0.7 | 0.7 | 0.9 | 0.7 | 0.6 | 0.9 | 0.8 | 0.8 | 0.8 | 0.7 | 0.8 | 0.7 | 0.7 | 0.9 | 0.7 | 0.8 |
| Zr | 149.9 | 127.3 | 166.3 | 147.2 | 127.9 | 164.5 | 158.3 | 162.2 | 165.3 | 161.7 | 89.8 | 88.1 | 89.5 | 103.9 | 83.8 | 77.5 |
| Hf | 4.0 | 3.4 | 4.3 | 3.8 | 3.4 | 4.2 | 4.1 | 4.2 | 4.2 | 4.1 | 2.7 | 2.5 | 2.6 | 3.1 | 2.4 | 2.4 |
| Pb | 22.5 | 17.6 | 22.4 | 10.4 | 18.8 | 8.7 | 15.5 | 19.7 | 13.8 | 19.7 | 47.1 | 42.9 | 62.8 | 17.6 | 19.9 | 15.6 |
| U | 2.0 | 1.8 | 1.9 | 1.8 | 1.6 | 1.6 | 1.7 | 1.6 | 1.7 | 1.7 | 1.8 | 1.7 | 1.7 | 2.3 | 1.7 | 1.8 |
| Th | 6.6 | 5.9 | 7.2 | 5.6 | 5.5 | 5.8 | 6.5 | 6.9 | 6.3 | 6.3 | 7.1 | 6.9 | 6.9 | 9.4 | 8.5 | 7.1 |
| La | 30.1 | 26.0 | 32.6 | 24.6 | 25.2 | 27.6 | 29.0 | 32.2 | 28.3 | 27.8 | 28.8 | 26.8 | 28.6 | 33.0 | 34.7 | 28.8 |
| Ce | 59.0 | 52.5 | 63.6 | 50.0 | 49.4 | 55.6 | 56.6 | 63.7 | 55.4 | 54.2 | 58.4 | 54.3 | 57.2 | 66.9 | 66.4 | 57.9 |
| Pr | 7.1 | 6.2 | 7.8 | 6.1 | 5.9 | 7.1 | 7.0 | 7.5 | 6.8 | 6.7 | 6.7 | 6.2 | 6.5 | 7.6 | 7.7 | 6.6 |

Table 1 (continued)

| | | | | | | | | | | | | | | | | |
|---|-------|-------|-------|-------|-------|-------|-------|-------|-------|-------|--------|-------|--------|-------|--------|--------|
| Nd | 27.0 | 23.4 | 30.0 | 23.7 | 22.4 | 28.9 | 26.9 | 29.1 | 26.6 | 26.0 | 25.8 | 24.0 | 25.5 | 29.4 | 29.5 | 25.8 |
| Sm | 4.6 | 4.0 | 5.3 | 4.3 | 3.9 | 5.8 | 4.8 | 4.9 | 4.8 | 4.7 | 4.9 | 4.7 | 4.8 | 5.3 | 5.2 | 4.8 |
| Eu | 1.4 | 1.2 | 1.5 | 1.2 | 1.2 | 1.7 | 1.4 | 1.4 | 1.4 | 1.3 | 1.4 | 1.3 | 1.3 | 1.4 | 1.4 | 1.3 |
| Gd | 3.5 | 3.0 | 4.1 | 3.5 | 3.0 | 5.0 | 3.8 | 3.6 | 3.8 | 3.6 | 4.0 | 4.1 | 4.0 | 4.4 | 3.8 | 4.0 |
| Tb | 0.5 | 0.4 | 0.6 | 0.5 | 0.4 | 0.7 | 0.5 | 0.5 | 0.5 | 0.5 | 0.6 | 0.6 | 0.6 | 0.6 | 0.4 | 0.6 |
| Dy | 2.5 | 2.0 | 2.9 | 2.7 | 2.1 | 4.1 | 2.6 | 2.3 | 2.6 | 2.5 | 2.7 | 2.7 | 2.7 | 3.4 | 1.8 | 2.6 |
| Ho | 0.4 | 0.4 | 0.5 | 0.5 | 0.4 | 0.7 | 0.4 | 0.4 | 0.4 | 0.4 | 0.5 | 0.5 | 0.5 | 0.6 | 0.3 | 0.5 |
| Er | 1.3 | 1.0 | 1.3 | 1.4 | 1.1 | 2.0 | 1.2 | 1.0 | 1.2 | 1.2 | 1.1 | 1.1 | 1.1 | 1.5 | 0.7 | 1.1 |
| Tm | 0.2 | 0.1 | 0.2 | 0.2 | 0.2 | 0.3 | 0.2 | 0.1 | 0.2 | 0.2 | 0.2 | 0.2 | 0.2 | 0.2 | 0.1 | 0.2 |
| Yb | 1.2 | 1.0 | 1.2 | 1.3 | 1.0 | 2.0 | 1.1 | 0.9 | 1.1 | 1.1 | 1.0 | 0.9 | 0.9 | 1.3 | 0.5 | 1.0 |
| Lu | 0.2 | 0.1 | 0.2 | 0.2 | 0.1 | 0.3 | 0.1 | 0.1 | 0.1 | 0.1 | 0.1 | 0.1 | 0.1 | 0.2 | 0.1 | 0.1 |
| Mg* | 44.60 | 54.30 | 31.54 | 46.77 | 44.80 | 35.71 | 35.06 | 23.30 | 32.66 | 34.12 | 35.85 | 34.78 | 35.67 | 33.13 | 30.21 | 31.11 |
| A/CNK | 1.82 | 1.89 | 1.54 | 2.02 | 1.80 | 1.63 | 1.57 | 1.59 | 1.47 | 1.51 | 1.78 | 1.78 | 1.78 | 1.54 | 1.68 | 1.54 |
| (La/Yb) _N | 17.32 | 18.41 | 18.92 | 13.16 | 17.06 | 9.46 | 17.93 | 24.69 | 18.11 | 17.96 | 19.96 | 20.21 | 21.55 | 16.98 | 51.27 | 20.62 |
| (Gd/Yb) _N | 2.41 | 2.53 | 2.82 | 2.24 | 2.39 | 2.03 | 2.76 | 3.32 | 2.88 | 2.80 | 3.33 | 3.65 | 3.63 | 2.72 | 6.65 | 3.42 |
| Eu/Eu* | 1.06 | 1.09 | 1.01 | 0.92 | 1.07 | 0.95 | 0.99 | 1.04 | 0.98 | 0.98 | 0.94 | 0.93 | 0.91 | 0.85 | 1.01 | 0.93 |
| ⁸⁷ Rb/ ⁸⁶ Sr _m | | | | | | | | | | | 0.3788 | | 0.3895 | | 0.9772 | 0.3461 |
| ⁸⁷ Sr/ ⁸⁶ Sr _m | | | | | | | | | | | 0.7097 | | 0.7100 | | 0.7131 | 0.7102 |
| ⁸⁷ Sr/ ⁸⁶ Sr ₂₉₁ | | | | | | | | | | | 0.7082 | | 0.7083 | | 0.7091 | 0.7088 |
| ¹⁴⁷ Sm/ ¹⁴⁴ Nd _m | | | | | | | | | | | 0.1144 | | 0.1147 | | 0.1057 | 0.1 |
| ¹⁴³ Nd/ ¹⁴⁴ Nd _m | | | | | | | | | | | 0.5122 | | 0.5122 | | 0.5121 | 0.5122 |
| εNd | | | | | | | | | | | -5.8 | | -5.9 | | -7.4 | -5.3 |
| T _{DM} (Ma) | | | | | | | | | | | 1613 | | 1625 | | 1627 | 1556 |

*Samples taken from Lago et al. (2004)

BDL below detection limit. Chondrite composition for normalisation from McDonough and Sun (1995). Sample location coordinates: UTM zone 30N

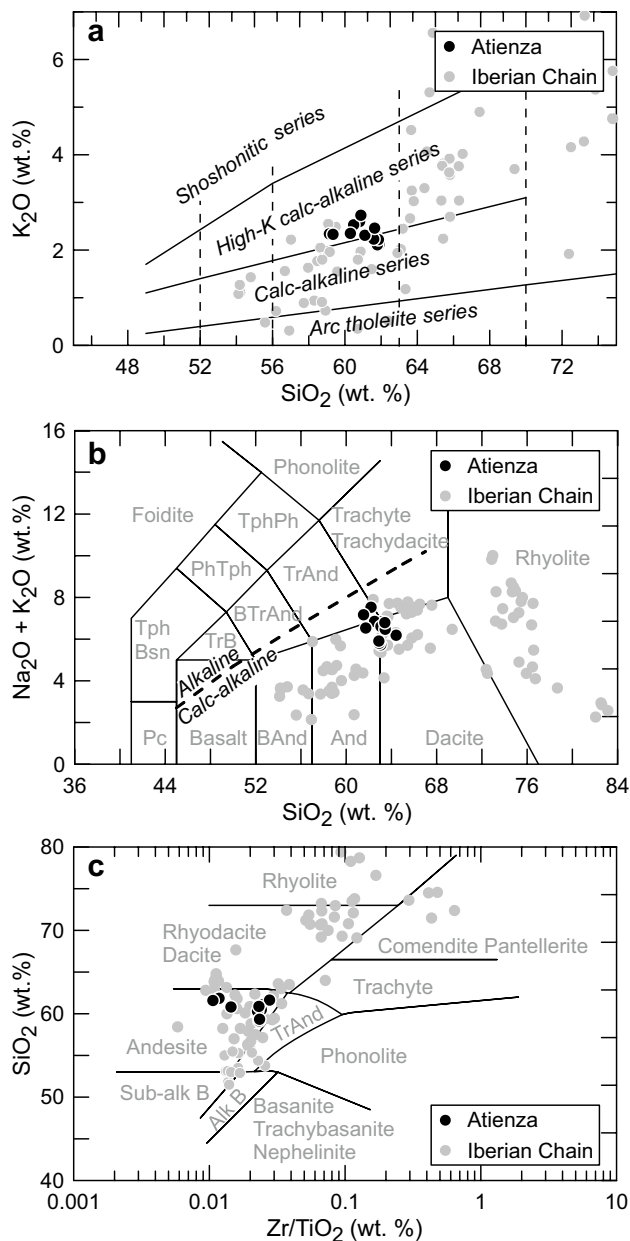


Fig. 5 Classification diagrams of the rocks of the Atienza magmatism. **a** SiO₂ vs K₂O diagram (Peccerillo & Taylor, 1976). **b** Alkalinity vs SiO₂ (TAS) diagram (Le Bas et al., 1986). **c** Zr/TiO₂ vs SiO₂ diagram (Winchester & Floyd, 1977). The grey points correspond to samples of the Permian magmatism in the Iberian Chain, taken from Lago et al. (2004) and references therein, Majarena et al. (2017), Navidad (1983), and Torres et al. (1991). *Alk B* Alkali basalt; *And* Andesite; *Band* Basaltic andesite; *Bsn* Basanite; *BTrAnd* Basaltic trachy-andesite; *Dac* Dacite; *Pc* Picro-basalt; *PhTph* Phono-tehrite; *Sub-alk B* Sub-alkali basalt; *Tph* Tephrite; *TphPh* Tephri-phonolite; *TrAnd* Trachy-andesite; *TrB* Trachy-basalt

The chondrite-normalised rare earth element (REE) patterns of these rocks are very similar (Fig. 6a), showing a strong enrichment in light rare earth elements (LREE), with (La/Yb)_N ranging between 16.98 and 24.69, and with no

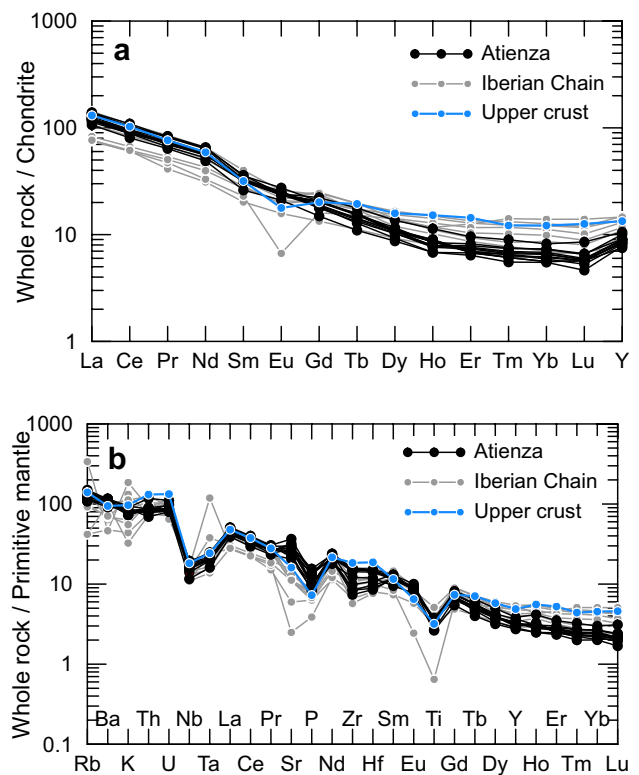


Fig. 6 Chondrite (a) and Primitive mantle-normalized (b) multi-element patterns for Atienza, the Permian magmatism of the Iberian Chain and the average composition of the upper crust. Composition of the Permian magmatism of the Iberian Chain taken from Lago et al. (2004) and references therein and Majarena et al. (2017). Composition of the upper crust from Rudnick and Gao (2003); compositions of Chondrite and Primitive mantle from McDonough and Sun (1995)

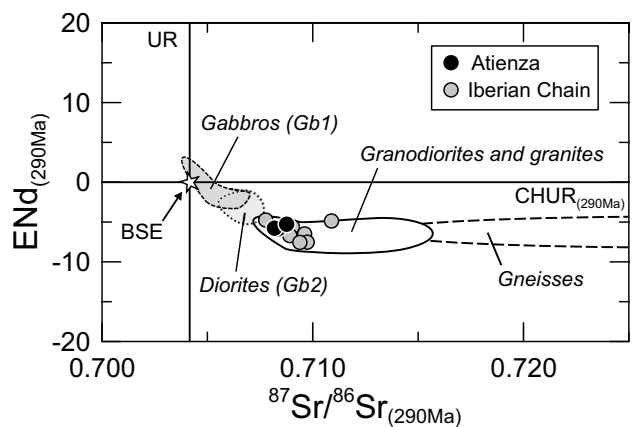


Fig. 7 ⁸⁷Sr/⁸⁶Sr (290) vs εNd (290) plot for the Permian igneous rocks of the Iberian Chain (Table 1). Data for comparison from the Spanish Central System (SCS) and the Pyrenees taken from Lemirre et al. (2019), Montero et al. (2017), Moreno et al. (1995), Orejana et al., (2009 and 2020), and Villaseca et al., (1998, 1999 and 2009). All data were recalculated to an age of 290 Ma. Abbreviations: Bulk Silicate Earth (BSE); Chondritic Uniform Reservoir (CHUR), Uniform Reservoir (UR)

significant Eu anomalies ($\text{Eu}/\text{Eu}^* = 0.85\text{--}1.07$). They also show moderate enrichment patterns in heavy rare earth elements (HREE) [$(\text{Gd}/\text{Yb})_{\text{N}} = 2.39\text{--}3.65$; Table 1, Fig. 6a].

Primitive mantle-normalised multi-element patterns (Fig. 6b) are also very similar and characterised by enrichment in large ion lithophile elements (LILE) (e.g., Rb, Ba) and light rare earth elements (LREE) and depletion in some of the high field strength elements (HFSE) (e.g., Nb, Ta). They also show a depletion in Ti and P and a small positive anomaly in Sr. In addition, the rocks exhibit a slight variability in Zr, Hf and the HREE (Fig. 6b).

The isotopic ratios analysed by Lago et al. (2004) in four samples of the sill (AT-6, AT-8, AT-12 and AT-13, Table 1) exhibit initial $^{87}\text{Sr}/^{86}\text{Sr}$ ratios of 0.70818 and 0.70875 and negative $\epsilon\text{Nd}(t)$ values of -5.9 to -5.3 (Fig. 7; Table 1), yielding a homogeneous Nd model-age of 1.6 Ga. The isotopic composition (Sr–Nd) of these rocks is similar to those of some Variscan and late-Variscan granites and granodiorites of the SCS (Moreno et al. 1995; Villaseca et al., 1999) and the Pyrenees (Lemirre et al., 2019), and it is close to the diorites and intermediate rocks of the SCS and the Pyrenees (Moreno and Rogers., 1995; Orejana et al., 2009 and 2020; Lemirre et al., 2019) (Fig. 7).

4.3 Mineral chemistry

Mineral analyses were performed in samples of both subvolcanic and volcanic rocks.

4.3.1 Plagioclase

The composition of the plagioclase phenocrysts ranges from labradorite (An_{58} , Ab_{41} , Or_1) to andesine (An_{36} , Ab_{62} , Or_3 ; Table 2, Supplementary material 1). The plagioclase phenocrysts have oscillatory zoning of high amplitude (anorthite content variations up to 16%) and low frequency (HALF; Viccaro et al., 2010). They usually have resorption horizons and Na-rich rounded cores that, in both cases, are overgrown by more anorthite-rich composition. Aside from these overgrowths and the oscillatory zoning, there are no apparent core-to-rim compositional variations. Plagioclase microcrysts of the matrix range from andesine (An_{45} , Ab_{53} , Or_2) to oligoclase (An_{20} , Ab_{72} , Or_8) and those of the coronas range from labradorite (An_{56} , Ab_{41} , Or_3) to oligoclase (An_{27} , Ab_{70} , Or_3).

4.3.2 Amphibole

The amphiboles are pargasite, magnesium-hastingsite and tschermakite, according to Leake et al. (1997)

(Supplementary material 1). The phenocrysts and the glomeroporphyritic crystals make up a heterogeneous crystal population with different compositions and zoning patterns. Therefore, three types of amphibole compositions have been defined based on their petrography and geochemistry: G, C, and M. In addition, amphibole microcrysts occur in the coronas.

The G-type amphiboles include crystals with glomeroporphyritic textures (Fig. 8a). This type shows the highest values (> 73.5) of mg^* [$100 \cdot \text{Mg}/(\text{Mg} + \text{Fe}^{2+} + \text{Fe}^{3+})$ atoms per formula unit, apfu] and CaO (> 11.5 wt.%; Fig. 9, Tables 2 and 3). We identified three zones in the G-type amphiboles: G_1 , G_2 and G_3 . The G_1 zone ($\text{mg}^* = 75.3\text{--}77.2$ and $\text{CaO} = 11.5\text{--}11.8$ wt.% Fig. 9, Tables 2 and 3) corresponds to the cores (Fig. 8a). The G_2 zone corresponds to the mantles that surround the G_1 cores (Fig. 5a). It is more magnesian ($\text{mg}^* = 77.6\text{--}79.8$) and calcic ($\text{CaO} = 11.6\text{--}12.1$ wt.%) than the G_1 zone (Fig. 9, Tables 2 and 3), forming reverse zoning. Finally, the G_3 zone is the external rim of the G-type amphiboles (Fig. 8a). This zone is less magnesian than the other zones ($\text{mg}^* = 73.5\text{--}77.2$) and has similar calcium content to the G_2 zone (11.5–12.1 wt.%) (Fig. 9, Tables 2 and 3).

The C-type compositions include cores (Fig. 8b, c) occurring in isolated phenocrysts. These cores have mg^* and CaO values ranging between 60.3 and 77.4 and 10.6 and 11.8 wt.%, respectively (Tables 2 and 3, Fig. 9). They show normal (C_{N}) or reverse zoning (C_{R}). The cores with normal zoning (C_{N} , Fig. 8b) have a higher value of mg^* (71.9–77.4) and CaO (11.1–11.8 wt.%) than the cores with reverse zoning (C_{R} : $\text{mg}^* = 61.3\text{--}71.7$; $\text{CaO} = 10.6\text{--}11.7$ wt.%). Moreover, the inner part of the C_{R} cores (Zone $\text{C}_{\text{R}1}$, Fig. 8c) is Fe-rich ($\text{mg}^* = 60.3\text{--}65.2$) and is surrounded by more magnesian compositions (Zone $\text{C}_{\text{R}2}$: $\text{mg}^* = 66.1\text{--}71.7$, Fig. 8c).

M-type compositions constitute the mantle of the phenocrysts with C-type cores (Fig. 8b, c), but sometimes they also form entire phenocrysts. They are the most common population and have been identified in all analysed samples. They are more evolved than C-type, with mg^* values between 47.7 and 71.3 and CaO between 9.2 and 12.4 wt.% (Fig. 9, Tables 2 and 3). The M-type is subdivided into two compositional zones, M_1 and M_2 . M_1 zone surrounds C-type compositions (Fig. 8c) and sometimes forms individual crystals. The mg^* values of the M_1 zone range between 56.1 and 71.3, and their CaO contents are between 10.4 and 11.8 wt.% (Fig. 9, Tables 2 and 3). M_2 zone surrounds C_{N} (Fig. 8b) and M_1 (Fig. 8c), and sometimes also forms entire crystals. This zone has the lowest values of $\text{mg}^* = 51.7\text{--}60.7$ and $\text{CaO} = 9.8\text{--}11.2$ wt.%.

Finally, the microcrysts of the coronas have a wide compositional variability, with mg^* values ranging between 53.4 and 67.8 and CaO between 9.5 and 12.4 wt.% (Fig. 9).

Table 2 Major element composition of representative mineral phases (see supplementary material 1 for structural formulae)

| Phase | Pl | Amp | | Bt | | | | Px | | Grt | | | | | | | | | | | | | | | | | | | | |
|--------------------------------|------------|------------|--------|----------------|----------------|----------------|----------------|-----------------|-----------------|----------------|----------------|-------|-------|-------|--------|--------|-----------|-----------|------------|-----------|-----------|------------|-----------|-----------|------------|--------|---------|--------|--------|-------|
| Sam- ple | ATU- D2 | ATU- D1 | ATU-D1 | ATU- D1 | ATU- D1 | ATU- D1 | ATU- D1 | ATU- D1 | ATU- D1 | ATU- D1 | ATU- D1 | | | | | | | | | | | | | | | | | | | |
| Type | Phen | Matrix | Corona | G ₁ | G ₂ | G ₃ | C _N | C _{R1} | C _{R2} | M ₁ | M ₂ | R | Phen | Rim | Corona | Phen | ATU- 4 | ATU- 9 | ATU- 12 | ATU- 4 | ATU- 9 | ATU- 12 | ATU- 4 | ATU- 9 | ATU- 12 | Corona | Igneous | Met | | |
| # | 204 | 119 | 117 | 55 | 57 | 123 | 6 | 196 | 198 | 200 | 9 | 53 | 210 | 100 | 21 | 184 | 50.85 | 49.54 | 49.54 | 49.54 | 49.54 | 49.54 | 49.54 | 49.54 | 49.54 | 49.54 | 49 | 72 | 101 | |
| SiO ₂ | 53.15 | 61.52 | 59.63 | 40.57 | 41.59 | 41.86 | 41.80 | 42.20 | 42.02 | 41.78 | 42.13 | 43.72 | 35.07 | 35.96 | 34.45 | 50.85 | 49.54 | 49.54 | 49.54 | 49.54 | 49.54 | 49.54 | 49.54 | 49.54 | 49.54 | 49.54 | 49.54 | 49.54 | 49.54 | 37.49 |
| TiO ₂ | 0.02 | 0.02 | 0.04 | 2.76 | 2.60 | 2.58 | 2.35 | 1.68 | 2.10 | 2.26 | 1.72 | 1.3 | 4.22 | 4.10 | 4.00 | 0.09 | 0.63 | 0.63 | 0.63 | 0.63 | 0.63 | 0.63 | 0.63 | 0.63 | 0.63 | 0.63 | 0.63 | 0.63 | 0.00 | |
| Al ₂ O ₃ | 29.58 | 23.88 | 24.41 | 14.34 | 14.06 | 13.97 | 15.24 | 14.99 | 15.01 | 12.83 | 12.65 | 10.86 | 16.68 | 16.10 | 16.79 | 0.91 | 4.08 | 4.08 | 4.08 | 4.08 | 4.08 | 4.08 | 4.08 | 4.08 | 4.08 | 4.08 | 4.08 | 4.08 | 22.39 | |
| MgO | 0.00 | 0.07 | 0.10 | 15.91 | 16.34 | 15.13 | 14.81 | 12.46 | 13.12 | 11.35 | 11.59 | 12.16 | 11.76 | 14.71 | 11.12 | 17.23 | 14.85 | 14.85 | 14.85 | 14.85 | 14.85 | 14.85 | 14.85 | 14.85 | 14.85 | 14.85 | 14.85 | 14.85 | 5.00 | |
| FeO _T | 0.07 | 0.33 | 0.66 | 9.43 | 8.40 | 9.72 | 9.13 | 12.81 | 10.71 | 15.81 | 16.51 | 16.93 | 18.99 | 14.18 | 19.72 | 29.85 | 8.65 | 8.65 | 8.65 | 8.65 | 8.65 | 8.65 | 8.65 | 8.65 | 8.65 | 8.65 | 8.65 | 27.89 | 32.24 | |
| MnO | 0.00 | 0.00 | 0.04 | 0.08 | 0.08 | 0.08 | 0.14 | 0.21 | 0.18 | 0.26 | 0.26 | 0.3 | 0.03 | 0.05 | 0.11 | 0.71 | 0.29 | 0.29 | 0.29 | 0.29 | 0.29 | 0.29 | 0.29 | 0.29 | 0.29 | 0.29 | 0.29 | 1.45 | 0.78 | |
| CaO | 11.86 | 5.55 | 6.58 | 11.84 | 12.07 | 11.51 | 11.72 | 11.06 | 11.25 | 10.93 | 10.41 | 9.89 | 0.15 | 0.02 | 0.05 | 0.53 | 21.36 | 21.36 | 21.36 | 21.36 | 21.36 | 21.36 | 21.36 | 21.36 | 21.36 | 21.36 | 21.36 | 5.71 | 2.01 | |
| Na ₂ O | 4.55 | 7.62 | 7.51 | 2.35 | 2.42 | 2.18 | 2.22 | 1.95 | 1.93 | 1.53 | 2.58 | 2.61 | 0.54 | 0.49 | 0.54 | 0.01 | 0.79 | 0.79 | 0.79 | 0.79 | 0.79 | 0.79 | 0.79 | 0.79 | 0.79 | 0.79 | 0.79 | 0.01 | 0.04 | |
| K ₂ O | 0.19 | 0.82 | 0.58 | 0.60 | 0.63 | 0.52 | 0.77 | 0.73 | 0.75 | 0.97 | 0.57 | 0.32 | 7.86 | 8.75 | 7.60 | 0.00 | 0.02 | 0.02 | 0.02 | 0.02 | 0.02 | 0.02 | 0.02 | 0.02 | 0.02 | 0.02 | 0.02 | n.d. | n.d. | |
| F | n.d. | n.d. | n.d. | 0.10 | 0.18 | 0.23 | 0.09 | 0.18 | 0.11 | 0.09 | 0.12 | 0.76 | 0.63 | 1.33 | 0.35 | n.d. | n.d. | n.d. | n.d. | n.d. | n.d. | n.d. | n.d. | n.d. | n.d. | n.d. | n.d. | n.d. | n.d. | n.d. |
| Cl | n.d. | n.d. | n.d. | 0.02 | 0.02 | 0.03 | 0.04 | 0.06 | 0.04 | 0.26 | 0.11 | 0.13 | 0.25 | 0.17 | 0.23 | n.d. | n.d. | n.d. | n.d. | n.d. | n.d. | n.d. | n.d. | n.d. | n.d. | n.d. | n.d. | n.d. | n.d. | n.d. |
| Total | 99.43 | 99.86 | 99.60 | 98.09 | 98.45 | 97.89 | 98.31 | 98.34 | 97.22 | 98.05 | 98.65 | 99.1 | 96.19 | 95.86 | 94.94 | 100.19 | 100.21 | 100.21 | 100.21 | 100.21 | 100.21 | 100.21 | 100.21 | 100.21 | 100.21 | 100.21 | 100.21 | 100.09 | 99.95 | |
| Class | An 58 | An 27 | An 32 | | | | | | | | | | | | | En 50 | En 42 | En 42 | En 42 | En 42 | En 42 | En 42 | En 42 | En 42 | En 42 | En 42 | En 42 | Pir 19 | Pir 20 | |
| | Ab 41 | Ab 68 | Ab 65 | | | | | | | | | | | | | Fs 49 | Fs 14 | Fs 14 | Fs 14 | Fs 14 | Fs 14 | Fs 14 | Fs 14 | Fs 14 | Fs 14 | Fs 14 | Fs 14 | Alm 62 | Alm 72 | |
| | Or 1 | Or 5 | Or 3 | | | | | | | | | | | | | Wo 1 | Wo 44 | Wo 44 | Wo 44 | Wo 44 | Wo 44 | Wo 44 | Wo 44 | Wo 44 | Wo 44 | Wo 44 | Gro 16 | Gro 8 | Gro 8 | |
| mg* | | | | 75.1 | 77.6 | 73.5 | 74.0 | 63.4 | 68.6 | 56.1 | 55.6 | 56.1 | 0.48 | 0.35 | 0.24 | 50.1 | 74.7 | 74.7 | 74.7 | 74.7 | 74.7 | 74.7 | 74.7 | 74.7 | 74.7 | 74.7 | 23.1 | 21.7 | 21.7 | |
| XFe | | | | | | | | | | | | | | | | | | | | | | | | | | | | | | |

FeO_T total Fe expressed as FeO

mg* is Mg-number (see text)

n.d. not determined

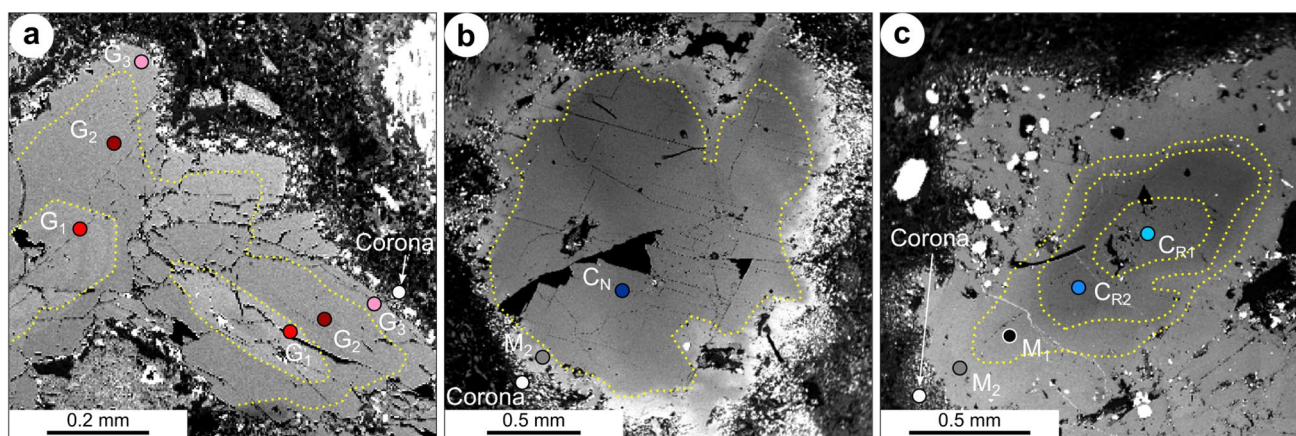


Fig. 8 Backscattered electron images of the amphiboles and their zoning. **a** Glomeroporphyritic amphibole. **b** Cores with normal zoning. **c** Cores with reverse zoning. The points indicate the composition of each type on the crystals

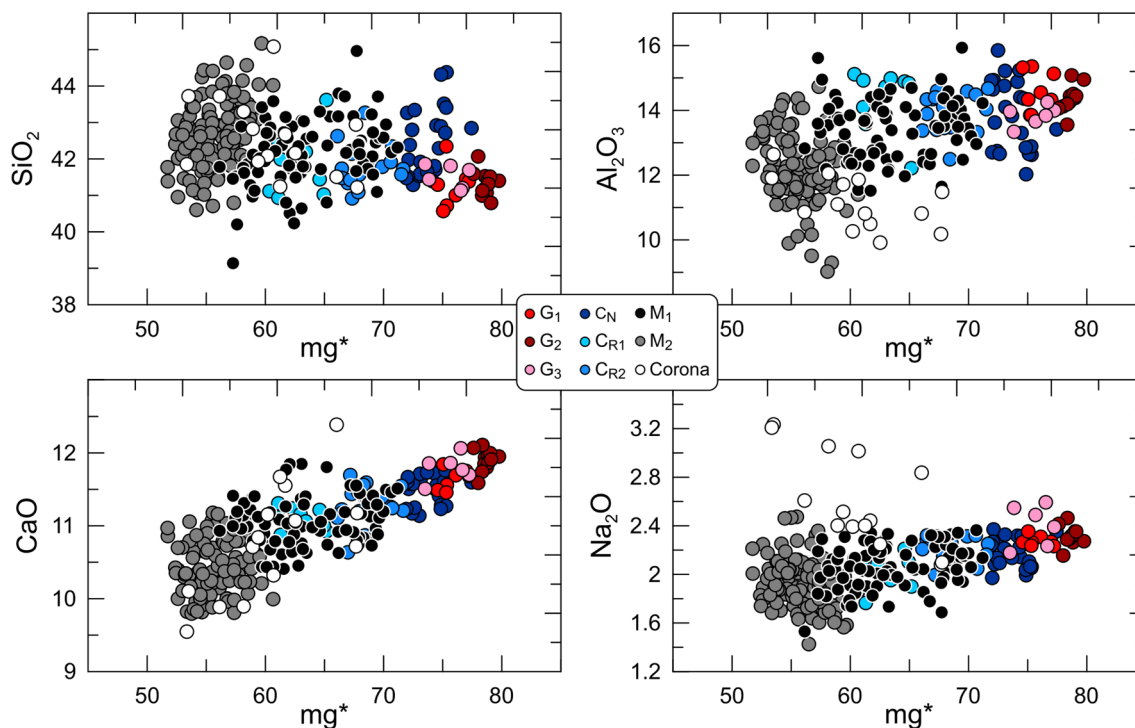


Fig. 9 Compositional variation of the defined types of amphibole. $mg^* = 100 * Mg / (Mg + Fe^{2+} + Fe^{3+})$

4.3.3 Biotite

Biotite has been divided into three compositional types. Type 1 includes biotite phenocrysts. They have a XFe [$Fe^{2+} / (Fe^{2+} + Mg)$ apfu] between 0.42 and 0.50, and Al^{IV} ranges between 1.24 and 1.4 (apfu) (Table 2, Supplementary material 1). Type 2 includes the rims of those phenocrysts, inclusions in amphibole, and pseudomorphs of amphibole. Their XFe values range between 0.26 and 0.4 and their Al^{IV} values

are similar to those of the type 1 (Table 2, Supplementary material 1). Finally, type 3 includes microcrystals developed from amphibole rims. They display XFe values ranging between 0.22 and 0.37 and fewer Al^{IV} values than the previous groups (1.07–1.24; Table 2, Supplementary material 1). The anhedral and resorbed biotites are not considered here because they are probably related to the xenoliths.

Table 3 Compositional and geothermobarometric results of the amphibole crystal population. The depth values have been calculated according to the density and crustal structure defined by Villaseca et al. (1999)

| Zone | G ₁ | G ₂ | G ₃ | C _N | C _{R1} | C _{R2} | M ₁ | M ₂ | R |
|------------|----------------|----------------|----------------|----------------|-----------------|-----------------|----------------|----------------|------------|
| CaO (wt.%) | 11.46–11.84 | 11.59–12.11 | 11.51–12.06 | 11.14–11.76 | 10.88–11.31 | 10.64–11.70 | 10.41–11.85 | 9.8–11.18 | 8.28–12.39 |
| mg* | 74.6–77.2 | 77.6–79.8 | 73.5–77.3 | 71.9–77.4 | 60.4–65.2 | 66.1–71.7 | 56.1–71.2 | 51.7–60.7 | 53.4–67.8 |
| T (°C) | 995±22 | 1010±22 | 1009±24 | 957±26 | 922±22 | 949±24 | 922±22 | 881±22 | – |
| P (kbar) | 7.8±1.8 | 8.0±1.5 | 7.8±1.3 | 6.1±1.8 | 5.3±0.6 | 5.8±1.4 | 4.9±0.9 | 3.8±0.8 | – |
| Depth (km) | 31±7 | 31±5 | 31±5 | 24±6 | 21±2 | 23±5 | 20±3 | 16±3 | – |
| # | 7 | 12 | 6 | 24 | 10 | 19 | 80 | 109 | 14 |

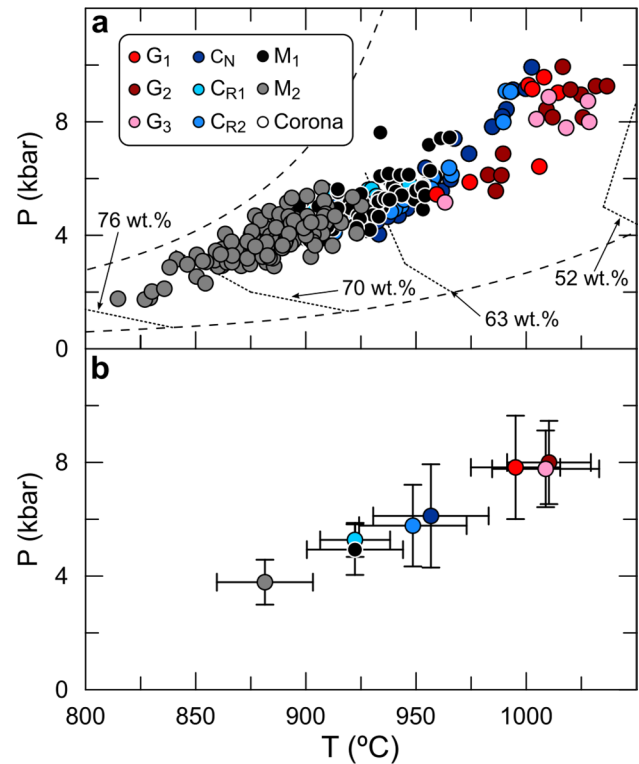


Fig. 10 P–T conditions of the studied amphiboles. **a** Estimated P–T conditions of crystallisation of the amphibole population on the basis of the equations of Ridolfi et al. (2021). The dashed lines indicate the stability conditions of the amphibole (Ridolfi et al., 2021) and the dotted lines show the anhydrous SiO₂ content (wt.%) of the melt in equilibrium with the amphibole at different P–T conditions (Ridolfi et al., 2010). **b** Average P and T for each type of amphibole. The bars indicate the standard deviation of the data

4.3.4 Pyroxene

The orthopyroxene has a very homogeneous composition (En₄₅₋₅₃, Fs₄₆₋₅₃, Wo₁), with mg* [100*Mg/(Mg + Fe²⁺ + Fe³⁺) apfu] values ranging between 47 and 54 (Table 2, Supplementary material 1). The clinopyroxene of the coronas of the amphiboles has an augite composition (En₄₂₋₄₀, Fs₂₅₋₁₃, Wo₄₅₋₃₃; Table 2, Supplementary material 1) with a wide range of mg* of 62–78.

4.3.5 Garnet

The garnets are, in all cases, almandine-rich (54.3–72.9 mol %) and grossular-poor (2.8–16.8 mol %), but they show a complex compositional evolution (Majarena et al., 2015a and 2021). The xenocrystic cores and the crystals from the metapelitic xenoliths share the same composition. They are characterised by low CaO (1.01–5.59 wt.%), high FeO_T (28.2–32.73 wt.%) and variable MnO (0.08–3.62 wt.%) and MgO (3.60–7.94 wt.%) (Supplementary material 1). Moreover, these xenocrystic

cores and crystals are zoned and show, from the core to the external area, an increase in FeO_T and MgO and a decrease in MnO and CaO. On the other hand, the igneous garnets have higher CaO (4.73–6.14 wt.%), slightly lower FeO_T (26.39–29.61 wt.%), MnO (0.21–2.37 wt.%), and MgO (4.49–5.60 wt.%), and show the opposite chemical zoning (MgO descent and CaO increase towards the rim) to the xenocrystic cores and garnets from xenoliths (Majarena et al., 2015a and 2021).

4.4 Geothermobarometry

The crystallisation pressures and temperatures of the amphiboles have been determined by applying the equations of Ridolfi (2021), that have an error of ± 22 °C and 0.2–2 kbar, and are based on the major elements of the amphibole and being independent of the whole-rock composition. The microcrysts of the coronas have not been considered for the P–T calculations as they are likely related to destabilisation processes.

We have obtained the highest values of pressure and temperature of crystallisation for the G-type amphiboles (Fig. 10a, b). They have very similar pressure (ca. 7.8 ± 1.8 kbar) and temperature (ca. 1005 ± 23 °C; Table 3), with a small increase in the temperature values from G₁ to G₂. The pressure and temperature obtained for C_N cores are 6.1 ± 1.8 kbar and 957 ± 26 °C (Fig. 10; Table 3), while the pressure and temperature obtained for C_R cores are lower (C_{R1}: 5.3 ± 0.6 kbar and 922 ± 22 °C; C_{R2}: 5.8 ± 1.4 kbar

and 949 ± 24 °C). The pressure obtained for the M₁ zone is 4.9 ± 0.9 kbar, and its temperature is 922 ± 22 °C (Table 3). Finally, we have obtained the lowest values of P (3.8 ± 0.8 kbar) and T (881 ± 22 °C) for the M₂ zone (Fig. 10; Table 3).

The igneous garnets are Ca-rich (CaO > 4 wt.%) and Mn-poor (Mn < 3 wt.%). This type of almandines could crystallise from hydrous andesitic magmas at more than 7 kbar and 900–950 °C and are unstable at shallow depths (Harangi et al., 2001 and references therein). Moreover, the experimental results of Green (1992) suggest that the mineral assemblage of plagioclase + amphibole + garnet in dacitic melts is stable at pressures above 8 kbar and temperatures above 800 °C.

Finally, the mineral assemblage of the xenoliths carried by these magmas (garnet + biotite + sillimanite + K-feldspar) is typical of amphibolite facies (2–8 kbar and 600–750 °C) (Bushmin & Glebovitsky, 2008).

4.5 LA-ICP-MS U/Pb geochronology

A total of 27 zircons from the sample ATUZ (Table 4) were analysed to determine the age of magma crystallisation. Only 16 zircons (11 analyses were discarded) with a degree of concordance of 95–105% were used for data reduction and ²⁰⁶Pb/²³⁸U age calculation (Table 4). To date the last crystallisation event, the analyses were performed in the outermost area of each crystal (Fig. 11a). They show oscillatory

Table 4 LA-ICP-MS U–Pb isotopic data from analysed zircons from Atienza magmatism

| Spot name | ²³⁸ U/ ²⁰⁶ Pb | 2 s | ²⁰⁷ Pb/ ²⁰⁶ Pb | 2 s | Rho | ²⁰⁶ Pb/ ²³⁸ U | 2 s | ²⁰⁷ Pb/ ²³⁵ U | 2 s | U | Th | Pb | Th/U | Conc. (%) |
|-----------|-------------------------------------|--------|--------------------------------------|--------|---------|-------------------------------------|-------|-------------------------------------|-------|-------|-------|-------|------|-----------|
| | | (abs) | | (abs) | | age | (abs) | age | (abs) | (ppm) | (ppm) | (ppm) | | |
| 24 | 21.5424 | 0.6497 | 0.0507 | 0.0022 | 0.2324 | 281.0 | 11 | 292.5 | 8.8 | 201 | 47.3 | 43.4 | 0.24 | 104% |
| 3 | 22.3314 | 0.6483 | 0.0523 | 0.0016 | 0.1471 | 282.8 | 8.7 | 282.3 | 8.2 | 333 | 95.5 | 85.4 | 0.29 | 100% |
| 18 | 22.3664 | 0.6503 | 0.0520 | 0.0013 | 0.2517 | 283.3 | 7.6 | 281.9 | 8.3 | 829 | 248 | 215 | 0.30 | 100% |
| 32 | 21.7108 | 0.6599 | 0.0516 | 0.0019 | 0.0748 | 283.6 | 10 | 290.2 | 8.6 | 279.8 | 58.2 | 49.9 | 0.21 | 102% |
| 21 | 22.0167 | 0.6302 | 0.0525 | 0.0020 | 0.2084 | 287.0 | 10 | 286.3 | 8.1 | 261 | 55.9 | 49.7 | 0.21 | 100% |
| 27 | 21.2314 | 0.6762 | 0.0517 | 0.0023 | 0.2718 | 289.0 | 12 | 296.6 | 9.1 | 159.6 | 35.5 | 32 | 0.22 | 103% |
| 15 | 21.645 | 0.7965 | 0.052 | 0.0023 | 0.16714 | 291.0 | 13 | 291 | 11 | 483 | 101.5 | 101 | 0.21 | 100% |
| 25 | 21.1149 | 0.6242 | 0.0520 | 0.0021 | 0.2864 | 292.1 | 11 | 298.3 | 8.9 | 170.8 | 31.5 | 27.7 | 0.18 | 102% |
| 5 | 21.4869 | 0.6925 | 0.0523 | 0.0018 | 0.0143 | 293.3 | 11 | 293.1 | 9.5 | 403 | 113 | 89.5 | 0.28 | 100% |
| 33 | 21.9539 | 0.6748 | 0.0537 | 0.0016 | 0.3306 | 294.0 | 8.4 | 287.1 | 8.4 | 508 | 62.1 | 54.6 | 0.12 | 98% |
| 14 | 21.3721 | 0.7308 | 0.0513 | 0.0033 | 0.10418 | 295.0 | 15 | 294.7 | 9.7 | 310 | 73.7 | 67.7 | 0.24 | 100% |
| 17 | 20.6569 | 0.5974 | 0.0526 | 0.0018 | 0.2333 | 305.0 | 9.8 | 304.7 | 8.9 | 379 | 67 | 67.1 | 0.18 | 100% |
| 13 | 20.5888 | 0.6359 | 0.0520 | 0.0021 | -0.0087 | 305.0 | 11 | 305.7 | 9 | 254 | 56.1 | 57.5 | 0.22 | 100% |
| 20 | 20.1939 | 0.6117 | 0.0520 | 0.0019 | 0.2669 | 306.4 | 11 | 311.5 | 9.5 | 275 | 60.7 | 60.2 | 0.22 | 102% |
| 12 | 19.4742 | 0.6068 | 0.0518 | 0.0013 | 0.0285 | 318.6 | 9 | 322.8 | 9.8 | 1260 | 171 | 169 | 0.14 | 101% |
| 19 | 19.5618 | 0.6123 | 0.0529 | 0.0014 | 0.2327 | 321.5 | 8.9 | 321.3 | 10 | 1201 | 157 | 138 | 0.13 | 100% |

Concordance of each analysis was calculated following Meinhold et al. (2010). Sample location coordinates: UTM zone 30N, X=506054 Y=4558613. Analyses used to calculate the Concordia age in italics

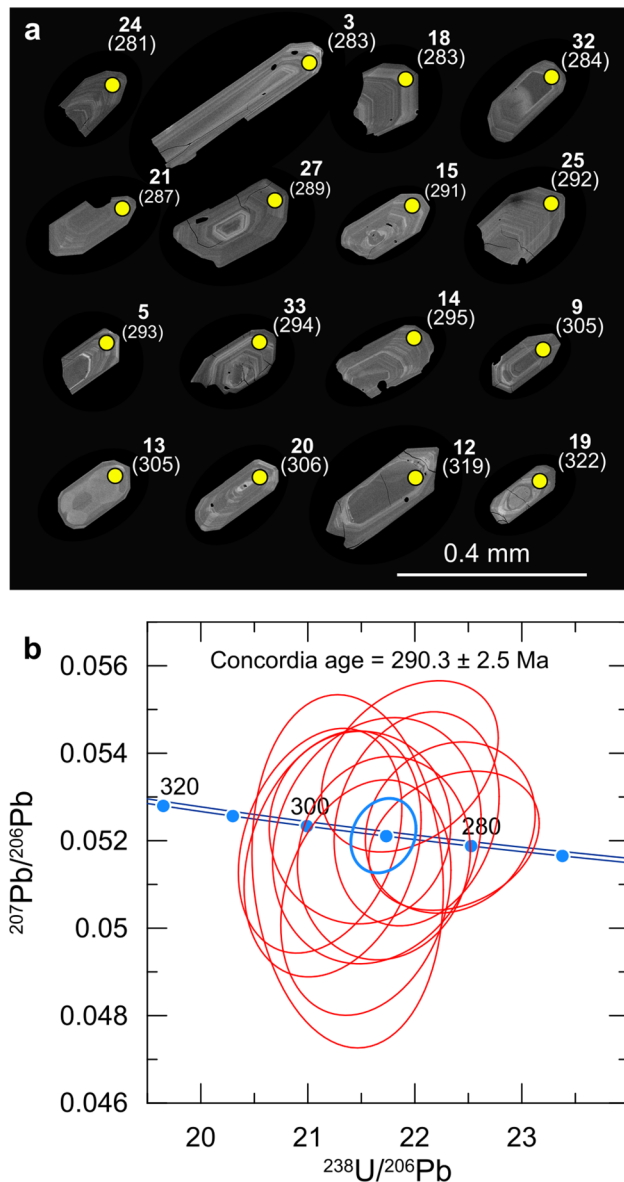


Fig. 11 **a** Cathodoluminescence images of the analysed zircons in the sill of Atienza. Labels indicate the test number and the $^{206}\text{Pb}/^{238}\text{U}$ age (Table 4). **b** Tera-Wasserburg plot (Tera & Wasserburg, 1972) of the analysed zircon crystals

concentric zoning and, in some cases, ovoidal cores truncated by the oscillatory zoning (Fig. 11a).

A Concordia age of 290 ± 3 Ma from a group of 11 concordant analyses was calculated (Fig. 11b, Table 4). A weighted average age of 288 ± 3 Ma was also obtained. The Th/U ratio of concordant analysis ranges from 0.12 to 0.30 (Table 4).

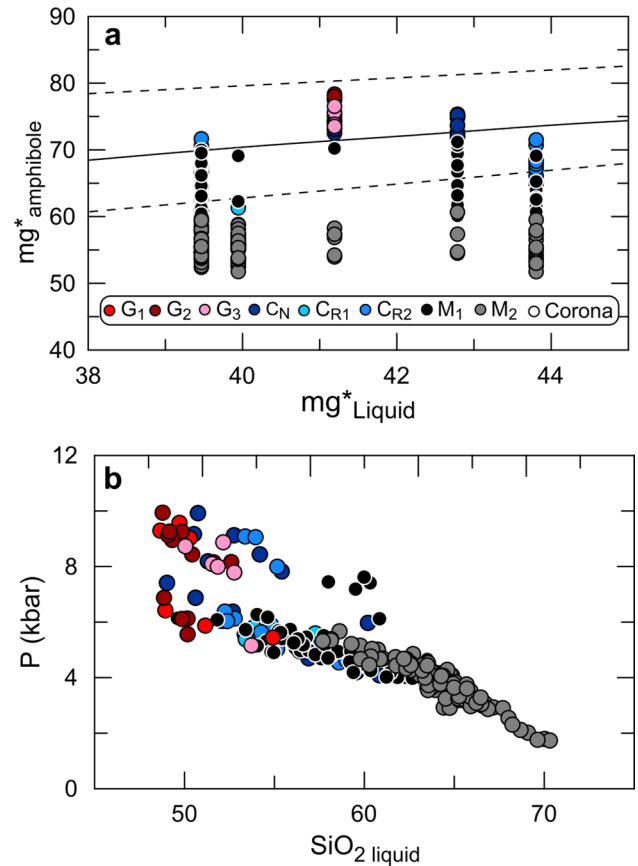


Fig. 12 **a** Equilibrium between the amphiboles and the melt. Solid and dashed lines (after Rhodes et al., 1979) represent the range of equilibrium between mineral and melt using an iron-magnesium distribution coefficient of 0.28 ± 0.11 (Putirka, 2016). The whole rock composition of the sample containing the mineral has been used as a proxy of the melt. **b** Relation between the estimated pressure of crystallisation of the amphibole population on the basis of the equations of Ridolfi et al. (2021), and the SiO_2 content (wt.%) of the melt in equilibrium with each amphibole composition (Putirka, 2016)

5 Discussion

5.1 Architecture of the magmatic plumbing system

The P–T crystallisation conditions, the observed compositional variations and the equilibrium/disequilibrium relationships between the minerals and the whole-rock, allow us to unravel a complex magmatic history for the Permian magmatism at Atienza.

The analysed amphiboles constitute a trend of decreasing Al_2O_3 , CaO and Na_2O with decreasing mg^* from the glomeroporphyritic crystals (G) to the outermost parts of the phenocrysts (M₂) (Fig. 9); in this variation trend, SiO_2 concentrations are fairly constant. On the other hand, the microcrystals of the coronas plot scattered and do not follow the same trend (Fig. 9).

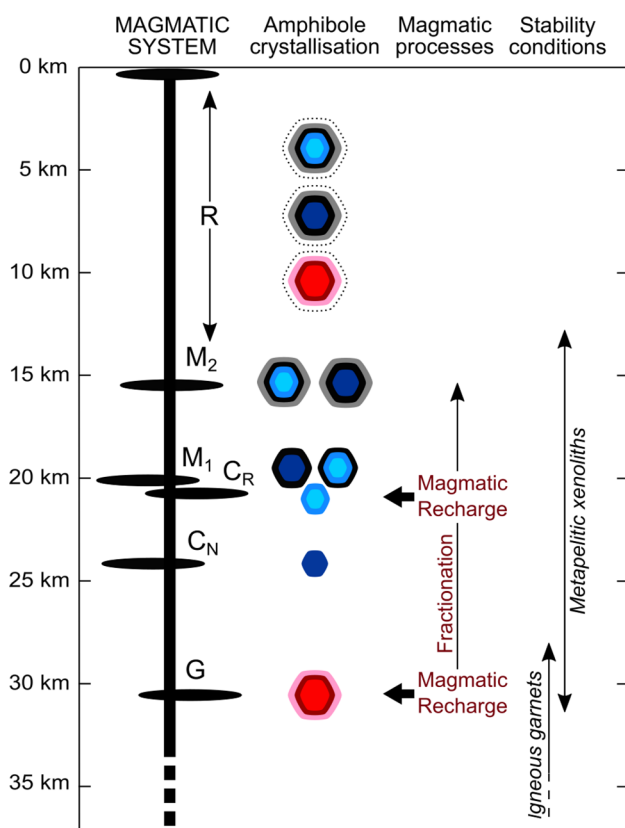


Fig. 13 Conceptual approach to the magmatic system and processes involved in the Atienza magmatism. The hexagons represent the different amphibole crystals (same legend as Figs. 5, 6 and 7). The depth values have been calculated according to the density and crustal structure defined by Villaseca et al. (1999)

The mineral-melt equilibrium between the amphibole and the whole-rock composition was assessed by applying the Rhodes diagram (Fig. 12a). They also show a continuous trend from compositions slightly more mafic than the whole-rock (G-Type) to more evolved than the whole-rock (M_2). The C_N amphiboles are in equilibrium with the whole-rock, whereas C_{R1} amphiboles are more evolved and C_{R2} amphiboles are close to the equilibrium (Fig. 12a). The M_1 amphiboles show a larger range of mg^* , from values near to the equilibrium to values clearly in disequilibrium.

Moreover, there is a direct relationship between the estimated pressures of crystallisation and the predicted SiO_2 content of the melt in equilibrium with the amphiboles (Fig. 12b). As the estimated pressure decreases, the melt in equilibrium with the amphiboles becomes more felsic (Fig. 12b). The compositional trend observed in the whole of the amphibole dataset (from G-Type to M_2 zones, Fig. 9) and the progressive descend in the SiO_2 of the melt in equilibrium with them (Fig. 12b) suggest that all of them belong to the same magmatic system and can be related by fractional crystallisation processes.

The glomeroporphyritic amphiboles (G-type), with a more primitive composition than the whole-rock (Fig. 12a), could correspond to primitive antecrysts. Regarding their internal zoning, the G_2 mantles have higher mg^* and CaO wt.% than the G_1 cores. In addition, the limit between the G_1 and G_2 zones is very clear, and the change of composition occurs abruptly. This compositional change from G_1 to G_2 suggests that the G_2 amphiboles grew after a more mafic and hotter magma recharge, which took place in the reservoir where G_1 type amphiboles were crystallising (Table 3, Fig. 13). Finally, the glomeroporphyritic amphiboles (G-type) evolved by fractional crystallisation from G_2 to G_3 forming normal zoning in the crystals. The P–T conditions obtained for the different zones of the G-Type amphiboles are very similar and show that they crystallised around 7.8 kbar and 1000°C (Table 3, Fig. 10b). These P–T conditions are consistent with those of the igneous garnets ($P > 7$ kbar and $T = 900$ – 950 °C; Harangi et al., 2001 and references therein). Moreover, the stability of the mineral assemblage of plagioclase + amphibole + garnet agrees with these pressures (Green, 1992). Considering the density of the crust (between 2.3 g/cm³ at the surface and 2.9 g/cm³ at a depth of 31 km) and the crustal structure in the CIZ defined by Villaseca et al. (1999), the estimated pressure of 7.8 kbar corresponds to a depth of 31 km (Table 3, Fig. 13).

Regarding the cores of the amphiboles, C_N crystallised at 6.1 kbar (24 km) and C_{R1} at 5.3 kbar (21 km). The C_{R2} have higher values of mg^* than C_{R1} (Fig. 9). This suggests, for G_2 zones, that C_{R2} grew after a more mafic and hotter magma recharge in the reservoir where C_{R1} were crystallising (Fig. 13). The observed pressure increase in the geothermobarometric results from C_{R1} to C_{R2} is unrealistic and only responds to the compositional change caused by the recharge. G-type amphiboles, C_N cores and C_R cores never occur together, suggesting that their crystallisation occurred in independent magma reservoirs (Fig. 13).

The magmatic recharges of a more basic melt inferred for the G_2 and C_{R2} amphiboles are consistent with the observed overgrown in the plagioclase crystals of the Na-rich rounded cores and the resorption horizons by a more anorthite-rich composition (Cashman & Blundy, 2013; Ruprecht & Wörner, 2007; Shcherbakov et al., 2011; Smith et al., 2009).

The M_1 amphiboles crystallised at 4.9 kbar (20 km). They surround both the C_N and C_R cores, indicating that the magmatic chamber where M_1 crystallised incorporated cores (C_N and C_R) formed at higher depths (Fig. 13). The crystallisation pressure of M_2 amphiboles was 3.8 kbar (16 km). They grew surrounding M_1 , C_N or C_R and evolved from M_1 by fractional crystallisation (Figs. 9, 12).

All amphibole crystals show resorbed rims or have microcrystalline coronas. The coronas reach a thickness of up to 100 μ m and contain microcrystals of amphiboles (R-type), biotite, clinopyroxene, plagioclase, apatite, ilmenite,

magnetite and titanomagnetite. The origin of this coronas has been related to decompression processes during a rapid rise of the magma (Buckley et al., 2006) that is coherent with the occurrence of Ca-bearing almandine, unstable at low pressures (Harangi et al., 2001), in these rocks. On the other hand, the biotite crystals of the coronas have a very similar composition to those that grow as amphibole pseudomorphs. This fact suggests a general destabilisation process in the amphibole that caused the formation of the coronas and the replacement of some amphibole crystals with biotite.

The range of crystallisation pressures of the amphiboles (3.8–7.8 kbar) agrees with the metamorphic conditions inferred for the metamorphic xenoliths carried by these magmas (2–8 kbar).

5.2 Origin of the magmatism

These rocks have nearly identical compositions and do not show any correlation of SiO_2 with other major oxides (Supplementary material 3). Nevertheless, fractional crystallisation is recorded by the evolution of the amphibole composition (Fig. 9). The rocks of Atienza are similar to those of the Permian calc-alkaline magmatism of the Iberian Chain but have higher LREE- and lower HREE-enrichment with respect to the chondrite composition (Fig. 6a). As amphibole has $D_{\text{mineral/melt}} > 1$ for HREE in andesites and dacites, the fractionation of this phase could be responsible for the differences in the REE-normalised patterns respect to the rest of the Permian calc-alkaline of the Iberian Chain.

Moreover, the moderate variability shown by Zr and Hf might be related to the zircon fractionation (Fig. 6b). On the other hand, the small positive anomaly of Sr in some rocks (Fig. 6b) could indicate slight plagioclase accumulation.

The accumulation of plagioclase and amphibole also could explain respectively the high content in LREE and HREE of some samples. In this sense, a correlation between the concentration in REE and the content in plagioclase and amphibole of the samples is observed. The sample with the highest content in REE (AT-11) have a slightly higher proportion of phenocrystals (*ca.* 45 vol.%) respect to the matrix (55 vol.%). The sample ATU-A9, with the lowest content in phenocrystals (*ca.* 35 vol.%) have the lowest concentration in REE. Finally, the sample ATU-A13, with a slightly higher concentration in plagioclase (*ca.* 60 vol.%) and a lower proportion of amphibole (*ca.* 25 vol.%), has in relation with the other samples, higher content in LREE and Sr, and lower content in HREE.

The negative anomalies in Nb, Ta, P and Ti and the enrichment in LILE (Fig. 6b) shown by these rocks suggest the involvement of crustal elements in the origin of this magmatism (Lago et al., 2004; Orejana et al., 2020). Their multi-elemental normalised patterns (REE and spider diagram, Fig. 6) are also very similar to that of the upper crust (Rudnick and Gao, 2003) in spite of their lower HREE content (that could be a result of amphibole and mainly garnet fractionation) and Zr and HF (that could be a result of zircon fractionation), and a higher content in Sr and P (that could be related, respectively, with the accumulation of plagioclase and apatite). Moreover, the occurrence of almandine garnet of igneous origin in these peraluminous rocks and metapelitic xenoliths is typical of melts generated by anatexis of metapelitic rocks (Harangi et al., 2001 and references therein). Finally, the Sr–Nd isotopic composition is markedly enriched ($\epsilon_{\text{Nd}} = -5.3$ to -5.9 ; $^{87}\text{Sr}/^{86}\text{Sr}_{(290 \text{ Ma})} = 0.7082$ to 0.7088 ; Table 1) and similar to some granites and granodiorites of the SCS and the Pyrenees, of crustal origin (Fig. 7).

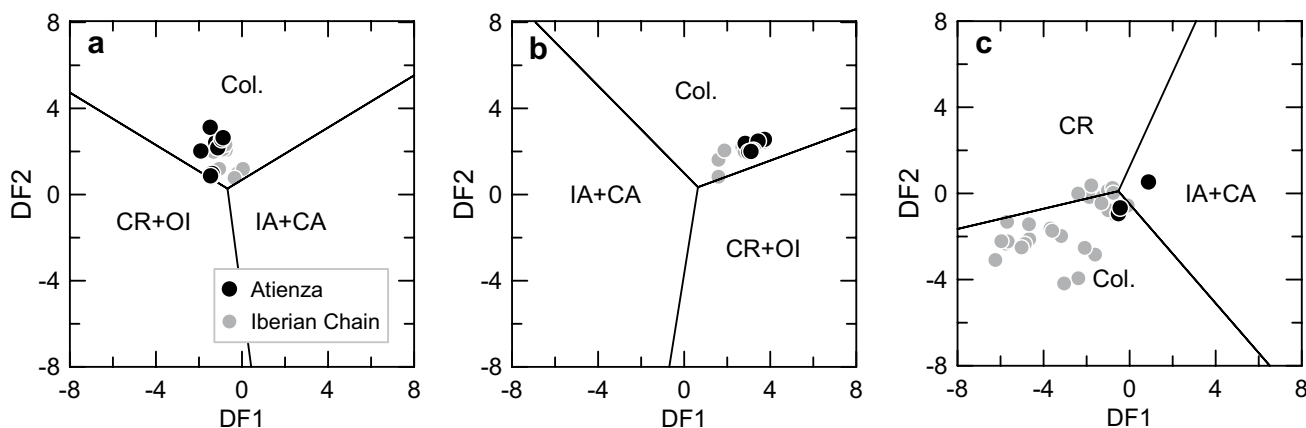


Fig. 14 Tectonic setting discrimination diagrams based on the whole rock composition for intermediate (a, b, Verma & Verma, 2013) and acid (c, Verma et al., 2012) rocks, according to the concentration of major (a, c) and immobile trace (b) elements. Col: collisional, IA island arc, CA continental arc, CR continental rift, OI ocean-island.

The grey points correspond to samples of the Permian magmatism in the Iberian Chain, taken from Lago et al. (2004) and the references therein, Majarena et al. (2017), Navidad (1983), and Torres et al. (1991)

All these elemental and isotopic criteria suggest a strong crustal imprint for the origin of this magmatism. The high concentration of partially reabsorbed enclaves of metapelite is consistent with this origin.

The Sr–Nd isotopic ratios are very similar to the rest of the Permian calc-alkaline rocks of the Iberian Chain (Fig. 7), supporting a similar petrogenesis. These rocks are close to the Gb2 magmatism of the SCS characterised by calc-alkaline microdioritic dyke swarms accompanied by felsic granitic porphyries of 292 Ma (Orejana et al., 2020; Villaseca et al., 2022). The microdiorite dyke swarms have been interpreted as the melting products of an enriched lithospheric mantle mixed locally with felsic magmas (Orejana et al., 2020). Assuming a mixing model between mantle-derived magmas and the crust (i.e. assimilation, anataxis) for the origin of the Permian magmatism as suggested for the rest of the Iberian Chain (Lago et al., 2004) and the coeval SCS magmatism (Orejana et al., 2020; Villaseca et al., 2022), in Atienza, the mantle signature is negligible, and the source of the melts could be close to the crust (Fig. 7).

The composition of these rocks plots in the field of collisional rocks (Fig. 14). This tectonic setting agrees with the palaeogeography of the Atienza area being part of the Gondwana continental plate, which collided with the Armorica, Avalonia and Laurussia plates during the end of the Variscan orogeny and led to the formation of the Pangea supercontinent (Pérez-Estaún et al., 2004; Wilson et al., 2004). This collision favoured the cortical thickening during the lifting of the Variscan orogen and the orocline folding of the Iberian Massif (Gutiérrez-Alonso et al., 2011). During the Cisuralian, a heat increase related to the thinning, delamination and subsidence of the lithosphere, and the asthenospheric rise in the Iberian Massif allowed melting in the crust and the lithospheric mantle, and the development of the Permian magmatism.

The depleted mantle (DM) model ages obtained with the isotopic compositions from Lago et al. (2004) range from 1.56 to 1.63 Ga (Table 1). These model ages are very similar to those of the granitoids and gneisses from the CIZ (Bea et al., 2010; Castro et al., 1999; Montero et al., 2017; Villaseca et al., 1998, 2009). These ages can be interpreted as an estimation of the time of crust formation (Rollinson & Pease, 2021). Nevertheless, no significant continental crust formation events in the SW of Europe and the N of Africa are known at this time, and the obtained ages could be due to the mixing of components with very different crustal residence times (Bea et al., 2011).

5.3 Age of the magmatism

The obtained age for the Atienza magmatism in this study is Sakmarian–Artinskian (290 ± 3 Ma, Fig. 11) and consistent with the previously obtained age by Hernando et al., (1980)

(287 ± 12 Ma, Asselian–Kungurian). As the age estimated in this work is within the error margin of Hernando et al., (1980) for the same sill but is more precise (± 4 My), we consider the age of 290 ± 3 Ma as the best estimation for the sill crystallisation age. In the Castilian Branch of the Iberian Chain, only two other outcrops of calc-alkaline magmatism have been dated: the pyroclastic flows of Orea and the Noguera de Albarracín sill. Both are located in the Albarracín massif and yield ages of 294 ± 3 Ma and 293 ± 2 Ma (Asselian–Sakmarian), respectively (Majarena et al., 2018). All these ages point to a short time range (290–294 Ma, *ca.* Sakmarian) for the development of this magmatism in the Castilian Branch.

In the Aragonese Branch, the Loscos gabbro (289 ± 1 Ma, Artinskian; Perini & Timmerman, 2008), the Cerro Redondo intrusion (285 ± 2 Ma; Artinskian; Majarena et al., 2017), and the Fombuena volcanoclastic deposit (283 ± 3 Ma, Artinskian–Kungurian; Conte et al., 1987) indicate an interval of 6 My (283–289 Ma, *ca.* Artinskian) for the development of the magmatism. The slight age difference between the radiometric ages of the magmatism in the Castilian Branch (290–294 Ma, *ca.* Sakmarian) and those of the Aragonese Branch (283–289 Ma, *ca.* Artinskian) suggests that, in the Iberian Chain, this magmatism is younger in the internal zones of the Variscan orogen, as indicated by Fernández-Suárez et al. (2000) and Gutiérrez-Alonso et al. (2011) for the Iberian Massif.

Moreover, the Permian calc-alkaline magmatism in the Iberian Chain can be considered as a short-live event (283–294 Ma) immediately after the formation of the Variscan orogen and the orocline folding of the Iberian massif (Gutiérrez-Alonso et al., 2011), that agrees with that observed in the rest of the WALZ (285–295 Ma; Fernández-Suárez et al., 2000). The calc-alkaline magmatism in the Iberian Cordillera is also contemporary with the calc-alkaline dykes of the SCS (292 Ma, Orejana et al., 2020) and the calc-alkaline volcanism of the Pyrenees (291–292 Ma, Pereira et al., 2014).

6 Conclusions

The magmatism of Atienza is characterised by calc-alkaline intermediate rocks with homogeneous compositions between andesite, dacite, trachyandesite and trachyte. They are porphyritic and contain phenocrysts of plagioclase, amphibole, biotite, garnet, orthopyroxene, xenocrysts of quartz and metapelite xenoliths.

We report for the first time a zircon U–Pb age of this magmatism (290 ± 3 Ma, Sakmarian–Artinskian). This age agrees with and better constrains the previous K–Ar in the whole-rock age of 287 ± 12 Ma (Asselian–Kungurian, Hernando et al., 1980) and coincides with the Cisuralian age of

the calc-alkaline magmatism in the Iberian Chain (Majarena et al., 2018 and references therein). This magmatism is coeval with other calc-alkaline magmatisms in the Pyrenees (Pereira et al., 2014), the Spanish Central System (Orejana et al., 2020) and the Iberian Massif (Gutiérrez-Alonso et al., 2011).

The negative anomalies in Nb, Ta, P and Ti, the enrichment in LILE, and the enriched Sr–Nd isotopic composition ($\epsilon_{\text{Nd}} = -5.3$ to -5.9 ; $^{87}\text{Sr}/^{86}\text{Sr}_{(290 \text{ Ma})} = 0.7082\text{--}0.7088$) suggest a strong crustal imprint for the origin of this magmatism. Moreover, the whole rock compositions are close to the upper crust. These rocks are also very similar to the rest of the Permian calc-alkaline rocks of the Iberian Chain, suggesting a similar origin. In a mixing model between mantle-derived magmas and the crust, previously proposed for the rest of the Iberian Chain and the coeval magmatism of the Spanish Central System, the source of the melts of the Atienza magmatism is close to the crust. At the beginning of the Permian, in the Iberian Massif, the lithospheric thinning and asthenospheric rise favoured the melting of the crust and the lithospheric mantle (Gutiérrez-Alonso et al., 2011).

The petrography and mineral chemistry and the geothermobarometric estimates led us to unravel the possible architecture of a magmatic system in the Iberian Chain for the first time. The deepest identified crystals are glomeroporphyritic amphiboles (G_1) crystallised around 31 km. This depth coincides with the stability conditions for the igneous garnet observed surrounding xenocrystic cores. At this level, recharge with more primitive magma induced reverse zoning (G_2) followed by fractional crystallisation (G_3). Most amphiboles have cores formed at 24 km (C_N), whereas the other cores are related to a magmatic mafic recharge and crystallised at 21 km (C_R). At a similar depth, the growth of the amphibole continued by forming mantles (M_1) that surrounded the cores and evolved by fractional crystallisation (M_2) up to 16 km depth. Finally, the rapid ascent of the magma produced the amphibole destabilization favouring the formation of microcrystalline coronas of amphibole, clinopyroxene, plagioclase, biotite, ilmenite, titanomagnetite and apatite, and the replacement of the amphibole by biotite. The magma and its crystal cargo were emplaced close to the surface as a subvolcanic sill and later dykes. Magma reaching the surface produced pyroclastic flows of blocks and ash.

Supplementary Information The online version contains supplementary material available at <https://doi.org/10.1007/s41513-023-00206-w>.

Acknowledgements The authors thank the technical and human support provided by SGIker of UPV/EHU and European funding (ERDF and ESF), the National Center for Electron Microscopy of the Complutense University of Madrid, and the Servicios de Apoyo a la Investigación (SAI) of the University of Zaragoza. This work is included in the scope of the predoctoral grant to Urbez Majarena (Operational Program

FSE Aragón 2014–2020, Gobierno de Aragón). This contribution was supported by the project PID2019-108753GB-C22 (MICINN, Spain) and the Aragón ERDF 2014–20 OP. We acknowledge the Gobierno de Aragón, supporting the Geotransfer-IUCA research group (E32_17R). This work greatly benefited from supportive and insightful reviews by Meritxell Aulinas, Teresa Ubide, and an anonymous reviewer.

Funding Open Access funding provided thanks to the CRUE-CSIC agreement with Springer Nature. The research leading to these results received funding from the Aragón government (Operational Program FSE Aragón 2014–2020; Geotransfer-IUCA research group: E32_17R, and project ERDF 2014–20 OP) and the Ministry of science and innovation of the government of Spain (project PID2019-108753GB-C22).

Data Availability Statement All data generated or analysed during this study are included in this published article (and its supplementary information files).

Declarations

Conflict of interest On behalf of all authors, the corresponding author states that there is no conflict of interest.

Open Access This article is licensed under a Creative Commons Attribution 4.0 International License, which permits use, sharing, adaptation, distribution and reproduction in any medium or format, as long as you give appropriate credit to the original author(s) and the source, provide a link to the Creative Commons licence, and indicate if changes were made. The images or other third party material in this article are included in the article's Creative Commons licence, unless indicated otherwise in a credit line to the material. If material is not included in the article's Creative Commons licence and your intended use is not permitted by statutory regulation or exceeds the permitted use, you will need to obtain permission directly from the copyright holder. To view a copy of this licence, visit <http://creativecommons.org/licenses/by/4.0/>.

References

- Álvaro, M. (1991). Tectónica. In: Instituto Tecnológico GeoMinero de España (Ed), Mapa Geológico de España 1:200.000. Hoja: 40 (7–5), Daroca (pp. 177–204).
- Álvaro, J. J., Bauluz, B., Gil-Imaz, A., & Ubide, T. (2018). $^{40}\text{Ar}/^{39}\text{Ar}$ chronological constraints on syn- and post-Variscan biotite porphyroblasts from the Iberian Chains, NE Spain. *Journal of Iberian Geology*, 44(4), 655–670. <https://doi.org/10.1007/s41513-018-0065-3>
- Ancochea, E., Hernán, F., & Vegas, R. (1981). Un marco tectónico para el Vulcanismo de Atienza (Provincia de Guadalajara). *Cuadernos Geología Ibérica*, 7, 421–430.
- Aparicio, A., & García-Cacho, L. (1984). Quimismo de los principales componentes minerales de las rocas volcánicas paleozoicas del área de Atienza (Provincia de Guadalajara). *Boletín Geológico y Minero*, 95(1), 80–89.
- Bea, F., Montero, P., Anbar, M. A., Molina, J. F., & Scarrow, J. H. (2011). The Bir Safsaf Precambrian inlier of South West Egypt revisited. A model for ~ 1.5 Ga TDM late Pan-African granite generation by crustal reworking. *Lithos*, 125(3–4), 897–914. <https://doi.org/10.1016/j.lithos.2011.05.004>
- Bea, F., Montero, P., Talavera, C., Abu Anbar, M., Scarrow, J. H., Molina, J. F., & Moreno, J. A. (2010). The palaeogeographic position of Central Iberia in Gondwana during the Ordovician:

- Evidence from zircon chronology and Nd isotopes. *Terra Nova*, 22(5), 341–346. <https://doi.org/10.1111/j.1365-3121.2010.00957.x>
- Buckley, V. J. E., Sparks, R. S. J., & Wood, B. J. (2006). Hornblende dehydration reactions during magma ascent at Soufrière Hills Volcano, Montserrat. *Contributions to Mineralogy and Petrology*, 151(2), 121–140. <https://doi.org/10.1007/s00410-005-0060-5>
- Bushmin, S. A., & Glebovitsky, V. A. (2008). Scheme of mineral facies of metamorphic rocks. *Geology of Ore Deposits*, 50(8), 659–669. <https://doi.org/10.1134/S1075701508080011>
- Calvín-Ballester, P., & Casas, A. (2013). Folded Variscan thrusts in the Herrera unit of the Iberian Range (NE Spain). *Geological Society of London, Special Publication*, 394(1), 39–52. <https://doi.org/10.1144/SP394.3>
- Cashman, K., & Blundy, J. (2013). Petrological cannibalism: The chemical and textural consequences of incremental magma body growth. *Contributions to Mineralogy and Petrology*, 166(3), 703–729. <https://doi.org/10.1007/s00410-013-0895-0>
- Castro, A., Douce, A. E. P., Corretgé, L. G., De La Rosa, J. D., El-Biad, M., & El-Hmidí, H. (1999). Origin of peraluminous granites and granodiorites, Iberian massif, Spain: An experimental test of granite petrogenesis. *Contributions to Mineralogy and Petrology*, 135(2), 255–276. <https://doi.org/10.1007/s004100050511>
- Conte, J. C., Gascón, F., Lago San José, M., & Carls, P. (1987). Materiales stephano-pérmicos en la fosa de Fombuena, Provincia de Zaragoza. *Boletín geológico y minero*, 98(4), 460–470
- Fernández-Suárez, J., Dunning, G. R., Jenner, G. A., & Gutiérrez-Alonso, G. (2000). Variscan collisional magmatism and deformation in NW Iberia: Constraints from U-Pb geochronology of granitoids. *Journal of the Geological Society*, 157(3), 565–576. <https://doi.org/10.1144/jgs.157.3.565>
- Gabaldón, V., Ruiz, P., Bascones, F., Martínez, F., & González, F. (1978). Mapa geológico de España 1:50.000, hoja nº 433 (Atienza) y memoria. IGME, Madrid, 45 p.
- Gorini, A., Ridolfi, F., Piscaglia, F., Taussi, M., & Renzulli, A. (2018). Application and reliability of calcic amphibole thermobarometry as inferred from calc-alkaline products of active geothermal areas in the Andes. *Journal of Volcanology and Geothermal Research*, 358, 58–76. <https://doi.org/10.1016/j.jvolgeores.2018.03.018>
- Green, T. H. (1992). Experimental phase equilibrium studies of garnet-bearing I-type volcanics and high-level intrusives from Northland, New Zealand. *Earth and Environmental Science Transactions of the Royal Society of Edinburgh*, 83(1–2), 429–438. <https://doi.org/10.1017/S0263593300008105>
- Gutiérrez-Alonso, G., Fernández-Suárez, J., Jeffries, T. E., Johnston, S. T., Pastor-Galán, D., Murphy, J. B., Piedad-Franco, M., & Gonzalo, J. C. (2011). Diachronous post-orogenic magmatism within a developing orocline in Iberia European Variscides. *Tectonics*. <https://doi.org/10.1029/2010TC002845>
- Harangi, S. Z., Downes, H., Kósa, L., Szabo, C. S., Thirlwall, M. F., Mason, P. R. D., & Mattey, D. (2001). Almandine garnet in calc-alkaline volcanic rocks of the Northern Pannonian Basin (Eastern–Central Europe): *Geochemistry, petrogenesis and geodynamic implications*. *Journal of Petrology*, 42(10), 1813–1843. <https://doi.org/10.1093/ptrology/42.10.1813>
- Hernán, E., Perni, A., & Ancochea, E. (1981). El vulcanismo del área de Atienza. *Estudios Geológicos*, 37, 13–25.
- Hernando, S. (1980). Mapa geológico del Pérmico y Triásico de la región Ayllón-Atienza. *Cuadernos De Geología Ibérica*, 6, 21–54.
- Hernando, S., Schott, J. J., Thuizat, R., & Montigny, R. (1980). Âge des andésites et des sédiments interstratifiés dans la région d'Atienza (Espagne). Etude stratigraphique, géochronologique et paléomagnétique. *Sciences Géologiques, bulletins et mémoires*, 32(2), 119–128.
- Jackson, S. E., Pearson, N. J., Griffin, W. L., & Belousova, E. A. (2004). The application of laser ablation-inductively coupled plasma-mass spectrometry to in situ U-Pb zircon geochronology. *Chemical Geology*, 211(1–2), 47–69. <https://doi.org/10.1016/j.chemgeo.2004.06.017>
- Julivert, M., & Martínez, F. J. (1983). Estructura de conjunto y visión global de la Cordillera Herciniana. In IGME (ed), Libro Jubilar JM Ríos, *Geología de España*. (pp. 612–630). IGME.
- Lago, M., Arranz, E., Pocoví, A., Galé, C., & Gil-Imaz, A. (2004). Lower Permian magmatism of the Iberian Chain Central Spain, Ant Its Relationship to Extensional Tectonics. *Geological Society of London Special Publications*, 223(1), 465–490. <https://doi.org/10.1144/GSL.SP.2004.223.01.20>
- Lago, M., Gil, A., Arranz, E., Galé, C., & Pocoví, A. (2005). Magmatism in the intracratonic Central Iberian basins during the Permian: Palaeoenvironmental consequences. *Palaeogeography, Palaeoclimatology, Palaeoecology*, 229(1), 83–103. <https://doi.org/10.1016/j.palaeo.2005.06.032>
- Le Bas, M. L., Maitre, R. L., Streckeisen, A., Zanettin, B., IUGS Subcommittee on the Systematics of Igneous Rocks. (1986). A subcommission classification of volcanic rocks based on the total alkalis-silica diagram. *Journal of Petrology*, 27(3), 745–750.
- Leake et al. (1997). Nomenclature of amphiboles: Report of the subcommittee on amphiboles of the International Mineralogical Association, Commission on New Minerals and Mineral Names. *The Canadian Mineralogist*, 35, 219–246
- Lemirre, B., Cochelin, B., Duchêne, S., de Saint Blanquat, M., & Pouljol, M. (2019). Origin and duration of late orogenic magmatism in the foreland of the Variscan belt (Lesponne—Chiroulet—Neouvielle area, french Pyrenees). *Lithos*, 336, 183–201. <https://doi.org/10.1016/j.lithos.2019.03.037>
- López-Gómez, J., Alónso-Azcárate, J., Arche, A., Arribas, J., Fernández Barrenechea, J., Borruel-Abadía, V., Bourquin, S., Cadenas, P., Cuevas, J., De la Horra, R., Bienvenido Díez, J., Escudero-Mozo, M. J., Fernández-Viejo, G., Galán-Abellán, B., Galé, C., Gaspar-Escribano, J., Gisbert Aguilar, J., Gómez-Gras, D., Goy, A & Viseras, C. (2019). Permian-triassic rifting stage. López-Gómez, J., Alónso-Azcárate, J., Arche, A., Arribas, J., Barrenechea, J. F., Borruel-Abadía, V., & Viseras, C. (2019). Permian-triassic rifting stage. In C. Quesada & J.T. Oliveira (Eds.), *The geology of Iberia: a geodynamic approach* (pp. 29–112). Springer, Cham. https://doi.org/10.1007/978-3-030-11295-0_3
- Ludwig, K. R. (2003). User's manual for Isoplot 3.0 a Geochronological toolkit for Excel. Berkeley Geochronological Center Special Publication 4 (71 pp.).
- Madinabeitia, S. G., Lorda, M. S., & Ibarra, J. G. (2008). Simultaneous determination of major to ultratrace elements in geological samples by fusion-dissolution and inductively coupled plasma mass spectrometry techniques. *Analytica Chimica Acta*, 625(2), 117–130. <https://doi.org/10.1016/j.aca.2008.07.024>
- Majarena, U., Galé, C., Lago, M., J. J. Esteban, E., de Madinabeitia, S. G., & Imaz, A. G. (2018). Edad Pb-Pb (LA-ICP-MS) de rocas ígneas postvariscas en la Sierra de Albarracín (Teruel-Guadalupe). *Teruel: Revista del Instituto de Estudios Turolenses*, 95(1), 7–19.
- Majarena, U., Galé, C., Lago, M., & Gil-Imaz, A. (2021). Los granates del magmatismo Cisuraliense en la Cordillera Ibérica: Origen, evolución y convergencia composicional a escala de cadena. *GeoTemas*, 18, 436–439.
- Majarena, U., Galé, C., Lago, M., Gil-Imaz, A., Ubide, T., & Larrea, P. (2015a). Los granates de las andesitas de Atienza: Consideraciones sobre su origen. *Macla*, 16, 89–90.
- Majarena, U., Gil-Imaz, A., Lago, M., & Galé, C. (2015b). El magmatismo pérmico del sector de Atienza (extremo W de la Cordillera

- Ibérica): Nuevos datos petro-estructurales para su interpretación genética. *Geogaceta*, 58, 63–66.
- Majarena, U., Lago, M., Galé, C., Esteban, J. J., García de Madinabeitia, S., & Gil-Imaz, A. (2017). El magmatismo Pérmico Inferior de la Sierra de Pardos (Rama Aragonesa de la Cordillera Ibérica, Zaragoza): Petrología y geoquímica. *Geogaceta*, 61, 111–114.
- Martínez Catalán, J. R., Martínez Poyatos, D. y Bea, F. (2004). In J. A. Vera (Ed), *Geología de España* (pp. 68–69). SGE-IGME, Madrid.
- McDonough, W. F., & Sun, S. S. (1995). The composition of the Earth. *Chemical Geology*, 120(3–4), 223–253.
- Meinhold, G., Kostopoulos, D., Frei, D., Himmerkus, F., & Reischmann, T. (2010). U-Pb LA-SF-ICP-MS zircon geochronology of the Serbo-Macedonian Massif, Greece: Palaeotectonic constraints for Gondwana-derived terranes in the Eastern Mediterranean. *International Journal of Earth Sciences*, 99(4), 813–832. <https://doi.org/10.1007/s00531-009-0425-5>
- Montero, P., Talavera, C., & Bea, F. (2017). Geochemical, isotopic, and zircon (U-Pb, O, Hf isotopes) evidence for the magmatic sources of the volcano-plutonic Olla de Sapo Formation, Central Iberia. *Geologica Acta*, 15(4), 245–260. <https://doi.org/10.1344/GeologicaActa2017.15.4.1>
- Moreno-Ventas, I., Rogers, G., & Castro, A. (1995). The role of hybridization in the genesis of Hercynian granitoids in the gredos massif, Spain: Inferences from Sr-Nd isotopes. *Contributions to Mineralogy and Petrology*, 120(2), 137–149.
- Navidad, M. (1983). *Vulcanismo Permo-Carbonífero en la Cordillera Ibérica (Rama Occidental)*. Fundación Juan March, Serie Universitaria 202(63).
- Orejana, D., Villaseca, C., & Kristoffersen, M. (2020). Geochemistry and geochronology of mafic rocks from the Spanish Central System: Constraints on the mantle evolution beneath central Spain. *Geoscience Frontiers*, 11(5), 1651–1667. <https://doi.org/10.1016/j.gsf.2020.01.002>
- Orejana, D., Villaseca, C., Pérez-Soba, C., López-García, J. A., & Billström, K. (2009). The Variscan gabbros from the Spanish Central System: A case for crustal recycling in the sub-continental lithospheric mantle? *Lithos*, 110(1–4), 262–276. <https://doi.org/10.1016/j.lithos.2009.01.003>
- Paton, C., Hellstrom, J., Paul, B., Woodhead, J., & Hergt, J. (2011). Iolite: Freeware for the visualisation and processing of mass spectrometric data. *Journal of Analytical Atomic Spectrometry*, 26(12), 2508–2518. <https://doi.org/10.1039/c1ja10172b>
- Peccerillo, A., & Taylor, S. R. (1976). Geochemistry of Eocene calc-alkaline volcanic rocks from the Kastamonu area, northern Turkey. *Contributions to Mineralogy and Petrology*, 58(1), 63–81.
- Pereira, M. F., Castro, A., Chichorro, M., Fernández, C., Diaz-Alvarado, J., Martí, J., & Rodríguez, C. (2014). Chronological link between deep-seated processes in magma chambers and eruptions: Permo-Carboniferous magmatism in the core of Pangaea (Southern Pyrenees). *Gondwana Research*, 25(1), 290–308. <https://doi.org/10.1016/j.gr.2013.03.009>
- Pérez-Estaún, A., Bea, F., Bastida, F., Marcos, A., Martínez-Catalán, J. R., Martínez-Poyatos, D., Arenas, R., Díaz-García, F., Azor, A., Simancas, J. F., & González-Lodeiro, F. (2004). La Cordillera Varisca europea: El macizo Ibérico. In: *Geología de España* (pp. 21–25). SGE-IGME, Madrid.
- Pérez-Mazarío, F. (1990). Estratigrafía de la unidad inferior del Pérmico del sector Atienza-Ujados (Borde Noreste del Sistema Central Español). *Revista de la Sociedad Geológica de España*, 3(3–4), 307–322.
- Perini, G., & Timmerman, M. J. (2008). Permian $^{40}\text{Ar}/^{39}\text{Ar}$ ages for post-Variscan minor intrusions in the Iberian range and Spanish central system. *Geologica Acta*, 6(4), 335–344. <https://doi.org/10.1344/105.000000261>
- Petrus, J. A., & Kamber, B. S. (2011). VisualAge: A novel approach to U-Pb LA-ICP-MS geochronology. *Mineralogical Magazine*, 75(3), 1633.
- Putirka, K. (2016). Amphibole thermometers and barometers for igneous systems and some implications for eruption mechanisms of felsic magmas at arc volcanoes. *American Mineralogist*, 101(4), 841–858. <https://doi.org/10.2138/am-2016-5506>
- Rhodes, J. M., Dungan, M. A., Blanchard, D. P., & Long, P. E. (1979). Magma mixing at mid-ocean ridges: Evidence from basalts drilled near 22 N on the Mid-Atlantic Ridge. *Tectonophysics*, 55(1–2), 35–61.
- Ridolfi, F. (2021). Amp-TB2: An updated model for calcic amphibole thermobarometry. *Minerals*, 11(3), 324. <https://doi.org/10.3390/min11030324>
- Ridolfi, F., Renzulli, A., & Puerini, M. (2010). Stability and chemical equilibrium of amphibole in calc-alkaline magmas: An overview, new thermobarometric formulations and application to subduction-related volcanoes. *Contributions to Mineralogy and Petrology*, 160(1), 45–66. <https://doi.org/10.1007/s00410-009-0465-7>
- Rollinson, H., & Pease, V. (2021). Radiogenic Isotopes in Geochronology. In *Using Geochemical Data* (pp. 178–193). Cambridge University Press. <https://doi.org/10.1017/9781108777834>
- Rudnick, R. L., Gao, S., Holland, H. D., & Turekian, K. K. (2003). Composition of the continental crust. In R. L. Rudnick (Ed.), *The crust* (pp. 1–64). Elsevier.
- Ruprecht, P., & Wörner, G. (2007). Variable regimes in magma systems documented in plagioclase zoning patterns: El Misti stratovolcano and Andahua monogenetic cones. *Journal of Volcanology and Geothermal Research*, 165(3–4), 142–162. <https://doi.org/10.1016/j.jvolgeores.2007.06.002>
- Shcherbakov, V. D., Plechov, P. Y., Izbekov, P. E., & Shipman, J. S. (2011). Plagioclase zoning as an indicator of magma processes at Bezymianny Volcano, Kamchatka. *Contributions to Mineralogy and Petrology*, 162(1), 83–99. <https://doi.org/10.1007/s00410-010-0584-1>
- Sláma, J., Košler, J., Condon, D. J., Crowley, J. L., Gerdes, A., Hancher, J. M., Matthew, S. S., Morris, G. A., Nasdala, L., Norberg, N., Schaltegger, U., Schone, B., Tubrett, M. N., & Whitehouse, M. J. (2008). Plešovice zircon: a new natural reference material for U-Pb and Hf isotopic microanalysis. *Chemical Geology*, 249(1–2), 1–35. <https://doi.org/10.1016/j.chemgeo.2007.11.005>
- Smith, V. C., Blundy, J. D., & Arce, J. L. (2009). A temporal record of magma accumulation and evolution beneath Nevado de Toluca, Mexico, preserved in plagioclase phenocrysts. *Journal of Petrology*, 50(3), 405–426. <https://doi.org/10.1093/petrology/egp005>
- Tejero, R., & Capote, R. (1987). La deformación hercínica en los Macizos Paleozoicos Nororientales de la Cordillera Ibérica. *Estudios Geológicos*, 43(5–6), 425–434.
- Tera, F., & Wasserburg, G. J. (1972). U-Th-Pb systematics in three Apollo 14 basalts and the problem of initial Pb in lunar rocks. *Earth and Planetary Science Letters*, 14(3), 281–304. [https://doi.org/10.1016/0012-821X\(72\)90128-8](https://doi.org/10.1016/0012-821X(72)90128-8)
- Torres, J. A., Lago, M., Pocoví, A., & Carls, P. (1991). Caracteres geológicos del magmatismo calco-alcalino: Stephaniense-Permico en el Anticlinal de Montalbán (provincia de Teruel). *Teruel: Revista del Instituto de Estudios Turolenses*, 82(1), 7–38.
- Torsvik, T. H., & Cocks, L. R. M. (2016). *Earth history and palaeogeography*. Cambridge University Press.
- Tunheng, A., & Hirata, T. (2004). Development of signal smoothing device for precise elemental analysis using laser ablation-ICP-mass spectrometry. *Journal of Analytical Atomic Spectrometry*, 19(7), 932–934. <https://doi.org/10.1039/B402493A>
- Ubide, T., Gale, C., Arranz, E., Lago, M., & Larrea, P. (2014). Clinopyroxene and amphibole crystal populations in a lamprophyre

- sill from the Catalonian Coastal Ranges (NE Spain): A record of magma history and a window to mineral-melt partitioning. *Lithos*, 184, 225–242. <https://doi.org/10.1016/j.lithos.2013.10.029>
- Verma, S. K., Pandarinath, K., & Verma, S. P. (2012). Statistical evaluation of tectonomagmatic discrimination diagrams for granitic rocks and proposal of new discriminant-function-based multi-dimensional diagrams for acid rocks. *International Geology Review*, 54(3), 325–347. <https://doi.org/10.1080/00206814.2010.543784>
- Verma, S. P., & Verma, S. K. (2013). First 15 probability-based multidimensional tectonic discrimination diagrams for intermediate magmas and their robustness against post-emplacement compositional changes and petrogenetic processes. *Turkish Journal of Earth Sciences*, 22(6), 931–995. <https://doi.org/10.3906/yer-1204-6>
- Viccaro, M., Giacomoni, P. P., Ferlito, C., & Cristofolini, R. (2010). Dynamics of magma supply at Mt Etna volcano (Southern Italy) as revealed by textural and compositional features of plagioclase phenocrysts. *Lithos*, 116(1–2), 77–91. <https://doi.org/10.1016/j.lithos.2009.12.012>
- Villaseca, C., Barbero, L., & Rogers, G. (1998). Crustal origin of Hercynian peraluminous granitic batholiths of Central Spain: Petrological, geochemical and isotopic (Sr, Nd) constraints. *Lithos*, 43(2), 55–79.
- Villaseca, C., Bellido, F., Pérez-Soba, C., & Billström, K. (2009). Multiple crustal sources for post-tectonic I-type granites in the Hercynian Iberian Belt. *Mineralogy and Petrology*, 96(3–4), 197–211. <https://doi.org/10.1007/s00710-009-0057-2>
- Villaseca, C., Downes, H., Pin, C., & Barbero, L. (1999). Nature and composition of the lower continental crust in central Spain and the granulite–granite linkage: Inferences from granulitic xenoliths. *Journal of Petrology*, 40(10), 1465–1496. <https://doi.org/10.1093/ptro/40.10.1465>
- Villaseca, C., Orejana, D., Higuera, P., Pérez-Soba, C., Serrano, J. G., & Lorenzo, S. (2022). The evolution of the subcontinental mantle beneath the Central Iberian Zone: Geochemical tracking of its mafic magmatism from the Neoproterozoic to the Cenozoic. *Earth-Science Reviews*, 228, 103997. <https://doi.org/10.1016/j.earscirev.2022.103997>
- Virgili, C., Hernando, S., Ramos, A., & Sopena, A. (1973). La sédimentation Permienne au centre de l'Espagne. *Compte rendu sommaire des séances de la Société géologique de France*, 15, 109–113.
- Wilson, M., Neumann, E. R., Davies, G. R., Timmerman, M. J., Heeremans, M., & Larsen, B.T. (2004). Permo-Carboniferous Magmatism and Rifting in Europe: introduction, in: Wilson, M, Neumann E.R., Davies, G.R., Timmerman M.J., Heeremans, M., Larsen, B.T. (Eds.), Permo-Carboniferous Magmatism and Rifting in Europe. *Geological Society of London Special Publications*, 223, 1–10. <https://doi.org/10.1144/GSL.SP.2004.223.01.01>
- Winchester, J. A., & Floyd, P. A. (1977). Geochemical discrimination of different magma series and their differentiation products using immobile elements. *Chemical Geology*, 20, 325–343. [https://doi.org/10.1016/0009-2541\(77\)90057-2](https://doi.org/10.1016/0009-2541(77)90057-2)